STUDY OF WAVEGUIDE OPTICAL ISOLATOR EMPLOYING NONRECIPROCAL RADIATION MODE CONVERSION FOR Si PHOTONICS

SALINEE CHOOWITSAKUNLERT

Student ID: nb16503

Major: Functional Control Systems

Supervisor

Prof. Hideki Yokoi

A thesis submitted in fulfilment of the

requirements for the award of the degree of

Doctor of Engineering

Shibaura Institute of Technology

CANDIDATE'S DECLARATION

It is hereby declared that this thesis or any part of it has not been submitted elsewhere for the award of any degree or diploma.

Signed: _____

(Salinee Choowitsakunlert)

Student No.: NB 16503

Certified by: _____

(Prof. Hideki Yokoi)

Dedicated

To

My honorable supervisor

Acknowledgements

Abstract

An optical isolator is an indispensable device in optical communication systems since it can protect active photonic devices from unwanted reflected light. Magnetic garnet crystals are necessary to construct the optical isolator owing to their large magneto-optic coefficient and low absorption loss in the near infrared region. In decade ago, optical isolators with a Si guiding layer have been researched widely. The author has investigated two types of the optical isolator with the Si guiding layer, employing a nonreciprocal guided-radiation mode conversion. First, the optical isolator utilizes a magneto-optic waveguide with a crystalline Si guiding layer. The magneto-optic waveguide is fabricated by bonding technique between a magnetic garnet and silicon-on-insulator (SOI) structure. Last, the optical isolator consists of an amorphous Si guiding layer deposited on a magnetic garnet cladding layer. Therefore, in both cases, the optical isolator is composed of a magneto-optic waveguide with the Si guiding layer and the magnetic garnet cladding layer.

In order to realize the magneto-optic waveguide with a crystalline Si guiding layer, surface activated bonding and adhesive bonding were considered. By using these techniques, Si and a magnetic garnet can be connected with each other at low temperature. The optical isolator employing the nonreciprocal guided-radiation mode conversion was designed at a wavelength of 1.55 μm. The nonreciprocal phase shift was calculated in the magneto-optic waveguide with a magnetic garnet / Si / SiO$_2$ structure. It was confirmed that the largest nonreciprocal phase shift was obtained when the thickness of the Si guiding layer is 200 nm. The relationship of waveguide parameters for isolator operation was investigated. By using bonding technique, there is concern over a gap generated between the Si guiding layer and the magnetic garnet cladding layer. The nonreciprocal phase shift was calculated when the gap existed in the magneto-optic waveguide and the relationship of waveguide parameters were clarified for various gaps. The magneto-optic waveguides were fabricated by surface activated bonding and adhesive bonding.

In the optical isolator with a hydrogenated amorphous Si (a-Si:H) guiding layer, the magneto-optic waveguide has a structure of air/ a-Si:H/ magnetic garnet. Since the a-Si:H guiding layer is deposited directly on the magnetic garnet cladding layer, there are no gaps between the a-Si:H and the magnetic garnet. The nonreciprocal phase shift was calculated at a wavelength of 1.55 μm and the relationship of waveguide parameters were clarified. The isolation ratio of the optical isolator was calculated by

simulating the electric field of TM guided mode and that of TE radiation mode. The magneto-optic waveguide with a-Si:H guiding layer was fabricated and evaluated.

The temperature dependence of the optical isolator employing a nonreciprocal guided-radiation mode conversion was investigated. The optical isolator consists of a rib-type magneto-optic waveguide with a-Si:H guiding layer. The relationship of rib height and rib width for the isolator operation was clarified for various operating temperatures. Refractive indices of layers in the magneto-optic waveguide were considered since proper refractive indices can circumvent deviation of the waveguide parameters due to the temperature shift. The results show that athermal operation can be achieved by the negative temperature dependence of the refractive index of the upper cladding layer, and the relationship of waveguide parameters varies only slightly with the selected upper cladding layer. As for the candidate of the upper cladding layer of the magneto-optic waveguide, TiO_2 and $C_6H_{11}CH_3$ compound were proposed for athermal operation of the optical isolator.

Contents

List of Figures

List of Tables

List of Publications

Journals

[1] S. Choowitsakunlert, T. Kobashigawa, N. Hosoya, R. Silapunt, H. Yokoi, "Temperature-insensitive design of waveguide isolator employing nonreciprocal guided-radiation mode conversion": Jpn. J. Appl. Phys., Vol. 57, no. 11, pp. 112201-1-112201-5, September 2018.

[2] S. Choowitsakunlert, K. Takagiwa, T. Kobashigawa, N. Hosoya, R. Silapunt, H. Yokoi, "Fabrication processes of SOI structure for optical nonreciprocal devices": Key Engineering Materials, Vol. 777, pp. 107-112, August 2018.

[3] S. Choowitsakunlert, K. Takagiwa, T. Kobashigawa, N. Hosoya, R. Silapunt, H. Yokoi, "Photosensitive adhesive bonding process of magnetooptic waveguides with Si guiding layer for optical nonreciprocal devices": Jpn. J. Appl. Phys., Vol. 57, no. 5, pp. 058007-1-058007-2, May 2018.

[4] S. Choowitsakunlert, R. Silapunt, and H. Yokoi, "A 1D study of antiferromagnetic operated on multiferroic composites in nano read head": Microsyst. Technol., March 2017. (online)

International Conferences

[1] N. Hosoya, S. Choowitsakunlert, R. Silapunt, H. Yokoi, "Magneto-optic waveguide with Si guiding layer for optical nonreciprocal devices using photosensitive adhesive bonding": 23rd Microoptics Conference, P-37, October 2018. 査読有り

[2] T. Kobashigawa, S. Choowitsakunlert, R. Silapunt, and H. Yokoi, "Athermal condition of nonreciprocal radiation type optical isolator using strip-loaded waveguide": 23rd Microoptics Conference, P-39, October 2018. 査読有り

[3] H. Yokoi and S. Choowitsakunlert, "Optical nonreciprocal devices for Si photonics": European Advanced Materials Conference 2018, Stockholm, Sweden, August 2018. 査読有り

[4]   S. Choowitsakunlert, R. Silapunt, H. Yokoi, "Magneto-optic waveguide in optical isolator employing nonreciprocal guided-radiation mode conversion for athermal operation": Advanced Photonics Congress 2018, JTu5A.2, July 2018. 査読有り

[5]   S. Choowitsakunlert, K. Takagiwa, T. Kobashigawa, N. Hosoya, R. Silapunt, H. Yokoi, "Fabrication processes of SOI structure for optical nonreciprocal devices": 7th International Conference on Advanced Materials and Engineering Materials, P3-104, May 2018. 査読有り

[6]   S. Choowitsakunlert, R. Silapunt, K. Takagiwa, H. Yokoi, "Athermal condition of magneto-optic waveguides in optical isolator employing nonreciprocal guided-radiation mode conversion": 22nd OptoElectronics and Communications Conference, P3-104, August 2017. 査読有り

[7]   S. Choowitsakunlert, K. Takagiwa, T. Kobashigawa, N. Hosoya, R. Silapunt, H. Yokoi, "Fabrication processes of magneto-optic waveguides with Si guiding layer for optical nonreciprocal devices": 5th International IEEE Workshop on Low Temperature Bonding for 3D Integration, 17SP-20, May 2017. 査読有り

[8]   S. Choowitsakunlert, K. Kobayayshi, K. Takagiwa, R. Silapunt, and H. Yokoi, "Design of optical isolator employing nonreciprocal radiation mode conversion for athermal operation": 21st Microoptics Conference, 13C-3, October 2016. 査読有り

[9]   K. Kobayashi, S. Choowitsakunlert, and H. Yokoi, "Optical isolator with Y_2O_3 strip-loaded waveguide employing nonreciprocal radiation mode conversion": 21st Microoptics Conference, 13C-4, October 2016. 査読有り

[10] H. Yokoi, S. Choowitsakunlert, K. Kobayashi, and T. Takagiwa, "Optical isolator with Si guiding layer fabricated by photosensitive adhesive bonding": 14th International Symposium on Semiconductor Wafer Bonding, H2-2094, Electrochem. Soc. Proc., October 2016. 査読有り

Domestic Conferences

[1] 松崎真悟, S. Choowitsakunlert, 小橋川卓矢, 細谷斉昭, R. Silapunt, 横井秀樹, "超音速フリージェット PVD 法を用いた Si フォトニクス用磁気光学導波路の設計": 第 6 回グリーンイノベーションシンポジウム, February 2019.

[2] 小橋川卓矢, S. Choowitsakunlert, R. Silapunt, 横井秀樹, "Si 導波層を有する磁気光学導波路の製作プロセスの検討": 第 5 回グリーンイノベーションシンポジウム, pp. 129-131, February 2018.

[3] 高際健児, S. Choowitsakunlert, 細谷斉昭, 横井秀樹, "a-Si:H/SiN$_x$導波層を有する磁気光学導波路の試作": 第 78 回応用物理学会学術講演会, 7p-PA2-13, September 2017.

[4] S. Choowitsakunlert, R. Silapunt, and H. Yokoi, "Multiferroic composites with PtMn sandwich structure for read head technology in 1D": 第 4 回グリーンイノベーションシンポジウム, pp. 91-93, February 2017.

[5] 高際健児, S. Choowitsakunlert, 細谷斉昭, 横井秀樹, "a-Si:H/SiN$_x$導波層を有する磁気光学導波路の設計および試作": nano tech 2017, February 2017.

CHAPTER 1 BACKGROUND

1.1 Introduction

Fiber-optic communication systems are light wave systems that employ optical fibers for information transmission. A basic optical fiber system consists of a transmitting device that converts an electrical signal into an optical signal, an optical fiber cable that carries the light, and a receiver that accepts the optical signal and converts it back into an electrical signal. A communication system transmits information from one place to another by transoceanic distance. Owing to the development of an optical fiber communication system, high speed processing for transmitting and receiving data is available.

The proficiency of waveguide devices is very important to develop the optical communication systems as in a semiconductor laser diode and an optical fiber. In 1960, T. Maiman operated the first optical maser, which is known as a laser [1]. He measured an emitted spectrum from a ruby. In 1962, laser action in a semiconductor material was demonstrated by R. Hall [2]. It took about another decade for the first semiconductor laser diodes to be developed that could operate at room temperature. After that, Diode Laser Labs of New Jersey introduced the first commercial room-temperature semiconductor laser diodes. The advent of high performance semiconductor laser diodes [3,4], high speed and high sensitivity photodetectors [5], and very low loss optical fibers [6-8] makes it reliable that optical fiber communications would be put into practical use, which is required from information society. As an optical transmission system is developing, the progress of the waveguide devices which construct the system is required. Besides, as electric circuits had progressed, the realization of optoelectronic integrated circuits has been heavily desired.

In 1969, S. E. Miller considered the concept of integrated optics [9-12]. The first idea of integrated optics was applied in thin film technology to form optical devices and circuit. It was found that a thin layer of dielectric film, which had larger refractive index than that of the surroundings, was a perfect optical waveguide. The purpose of integrated optics is to unify many optical components on a single chip. The integrated optics has been used frequently to denote waveguide devices on transparent substrates, such as glass or lithium niobate ($LiNbO_3$). The initial yields were very poor for a single chip

so that it seemed foolhardy to decrease the problem by placing on a chip. Nevertheless, in 1954, a chip with four-transistor circuit was investigated, that included some passive circuit elements, connected by external wire bonds. In 1978, the first demonstration of integrated optics [13] was reported, which was an integration of an injection laser diode and a Gunn oscillator. Meanwhile, the Photonic Integrated Circuit (PIC) [14] has been introduced to describe semiconductor integrated devices. The PIC is a device that integrates multiple photonic functions and as such is similar to an electronic integrated circuit. The major difference between the two circuits is that a PIC provides function for information signals imposed on optical wavelengths typically in the visible spectrum or near infrared from 850 nm to 1650 nm. The most commercially utilized material platform for PICs is indium phosphide (InP), which allows the integration of various optically active and passive functions on the same chip. In 1990, the PIC was demonstrated with indium gallium arsenide (GaInAs)/ gallium indium arsenide phosphide (GaInAsP) multiple-quantum-well integrated heterodyne receiver [15]. The characteristics of PICs are the stability against mechanical vibration or thermal fluctuation, low operating voltage, high speed operation, small in size, and suitable for mass production.

In order to maintain a performance of optical communication systems, the characteristic of the semiconductor laser diodes plays a very important roll. Semiconductor laser diodes are available as reliable light source. The rapid development of optical fiber communication systems requires a high level of on-chip integration of various optical components. Optical integration does not have the same degree of success as electronics integration. The semiconductor laser diodes are usually fabricated on III-V compound semiconductor wafers such as gallium arsenide (GaAs) and InP.

It is essential that the laser is protected from reflected light, otherwise they can become unstable or can even be damaged. An external feedback gives effect by the enhanced effect of carrier vibration [16-17], mode hopping phenomena among external cavity modes [18], a transition to chaotic state [19-20], effect of coherence collapse [21], and so on. In optical communication systems, optical isolators are one of the most important passive components [22]. Another type of passive element that is commonly used in fiber optic systems is an *optical circulator* [23]. The function of an optical isolator and an optical circulator are to let a light beam pass through in one direction, that is, the forward direction only, like a one-way traffic. Therefore, optical isolators are used to prevent destabilizing feedback of light that causes undesirable effects such as frequency instability in laser sources and parasitic oscillation in optical amplifiers. Ordinary optical isolators are commercially available which make use of the Faraday effect to produce nonreciprocity. The Faraday effect is a magneto-optic phenomenon in which the polarization plane of light passing through a transparent substance is rotated in the presence of a

magnetic field parallel to the direction of light propagation. The magnitude of the rotation depends on the strength of the magnetic field and the nature of the transmitting substance. Unlike in the optical activity (or natural activity), the direction of the rotation changes its sign for light propagating in reverse. For example, if the ray transverses the same path twice in opposite direction, the total rotation is double of the rotation for a single passage.

1.2 Optical nonreciprocal devices

Several kinds of the optical nonreciprocal device are investigated with the magneto-optic waveguide. The design of the optical nonreciprocal devices will be explained.

1.2.1   Bulk optical isolator

An optical isolator plays an important role in stabilizing optical communication systems by eliminating the back reflection of each device. Currently, a bulk optical isolator dominates in optical communications compared with in-line or waveguide ones. A number of configurations for polarization-dependent and polarization-independent optical isolator have been proposed and demonstrated [24,25].

1.2.1.1 Polarization-dependent type

The optical isolators are common and their design is fairly well understood for bulk devices. Generally, optical isolators consist of a magnetic garnet that shows large Faraday effect, a permanent magnet for applying an external magnetic field, and polarizing elements with polarization axis offset of 45 degrees as shown in figure 1.1. In forward propagation, the light passing the optical isolator undergoes by following: at first the light passes through the polarizer. The incident light is transformed into a linearly polarized light. After it passes through the Faraday rotator, the polarization plane is rotated by 45 degrees. Then, this light passes through the analyzer without loss since its polarization plane is now in the same direction as the light transmission axis of the analyzer. On the other hand, a backward light propagates in a slightly different manner. The light passing through the analyzer is transformed into a linearly polarized light with a 45 degrees-tilt in the transmission axis. Passing through the Faraday

rotator, the polarization plane of the backward light is rotated by 45 degrees in the same direction as the first round. Therefore, this light is completely shut out by the polarizer because its polarization plane is now 90 degrees away from the light transmission axis of the polarizer. The performance of optical isolators is primarily evaluated by their insertion losses and isolation ratio (the ratio of the optical power propagating backward at the input to the forward power at the output), both of which are determined by the absorption losses end-face reflectance and the extinction ratios of optical elements.
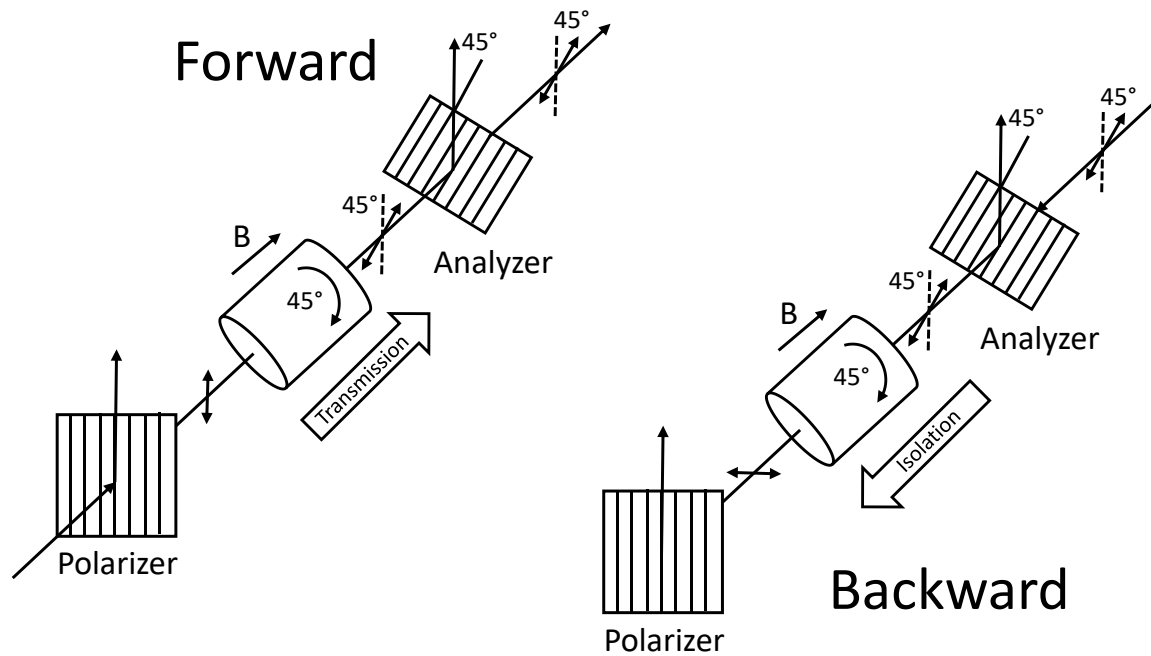
Figure 1.1 Operation principle of a bulk-type optical isolator.

1.2.1.2 Polarization-independent type

While polarization-dependent optical isolators operate for the light polarized, only in a specific direction, polarization-independent isolators operate for any kind of polarization state. Consequently, these isolators are frequently used in optical fiber amplifiers. The basic working principle of a polarization-independent optical isolator was first proposed by T. Matsumoto [26]. Its arrangement consists of a Faraday rotator and a half-wave plate inserted between a pair of birefringent crystal plates of equal thickness (as spatial walk-off polarizer, SWP). The birefringent plate functions to split the incident beam into a pair of orthogonal rays and separate one ray ("E" ray) from the other ray ("O" ray) as they travel through the plate. This phenomenon of spatial displacement is often referred to as "walk off". The two separated components are rotated as they pass through the half-wave plate and the Faraday

rotator, and then enter the second birefringent plate where they are recombined to form the output signal. Since a Faraday rotator is a nonreciprocal device, any signal traveling in the reverse direction through the isolator will be physically separated into orthogonally polarized signals as it passes through both birefringent plates and will not be recombined into the input fiber. In an alternative design, a wedge-shaped spatial walk-off polarizer was used to bring a large separation of two polarization states in backward direction by Shirasaki. The schematic and working principle is depicted in figure 1.2.
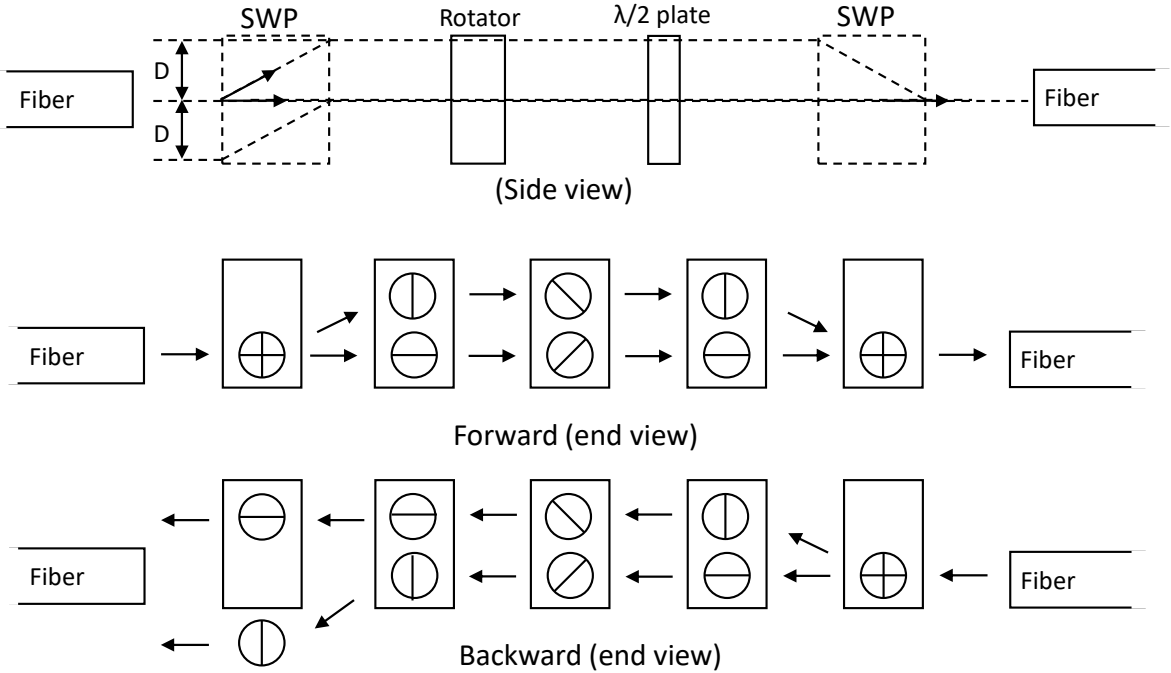
Figure 1.2 The diagram of fiber-embedded polarization-independent isolator

1.2.2   Waveguide optical isolator

The bulk isolator is not suitable for integrating with other optical devices. Waveguide optical isolators have been investigated to realize the integrated circuit. There are a few basic concepts to construct the waveguide optical isolator. They utilize a mode conversion which corresponds to the Faraday rotation in a bulk isolator, an optical nonreciprocal phase shift which occurs in transverse magnetic (TM) modes, and a mode coupling between guided and radiation modes.

A mode-conversion type optical isolator consists of three parts that include input polarizer, Faraday rotator, and output polarizer. The Faraday rotator composes of a magnetic garnet such as yttrium iron

garnet and terbium gallium garnet, which have large Faraday rotation coefficient, placed in a cylindrical permanent magnet and rotates the polarization of passing light by 45 degrees. In forward direction, the light will propagate passing input polarizer and the polarized light will have only one direction (vertical plane). Then, the light passes through the Faraday rotation, so that the plane of polarization will be rotated 45 degrees. The output polarizer, which is aligned 45 degrees relating to the input polarizer, will then let the light pass through. On the other hand, light traveling in the reverse direction (backward direction) will pass through the output polarizer and become polarized by 45 degrees. The light passes through the Faraday rotator and experiences additional 45 degrees of non-reciprocal rotation. The light is now polarized in the horizontal plane and will be rejected by the input polarizer, which allows light polarized in the vertical plane to pass through. Owing to this principle, the device acts as a bulk-type optical isolator.

Waveguide modes in planar dielectric waveguides have their electric vector vibrating in orthogonal planes. This device includes two polarizers that are difficult to set rotation angle at 45 degrees, therefore, an optical active element must be prepared. An optical isolator with parallel polarizers is employing the mode conversion by using Faraday rotation as shown in figure 1.3. The electric vectors are 0 degree or 90 degrees plane by the active element. It is possible to replace the active element with an anisotropic one in the waveguide cases because TM modes have a component of electric field along the propagation direction and an anisotropic crystal can be oriented to provide a coupling between this field component and the electric field of transverse electric (TE) modes as shown in figure 1.4. When this principle is applied to the waveguide optical isolator, propagation constants of TE and TM modes must be coincident for obtaining mode conversion between two modes. It is difficult to realize the waveguide optical isolator employing the mode conversion. The phase matching between two modes is a coincidence in propagation constants of the two modes. Figure 1.5 shows another waveguide-type optical isolator employ mode conversion. J.P. Castera et al. proposed a similar isolator using the Faraday and Cotton-Mouton effects [27]. These waveguide designs required mode conversion that was similar to that used in bulk isolators, but they needed to match TE and TM propagation constants by fine-tuning the waveguide dimensions which was difficult with the lithography of the time. Therefore, in 1980s, they continued to focus on complete elimination of birefringence to enable waveguides to exhibit full Faraday rotation. Ando et al. [28] proposed a compact tandem (Faraday/Cotton-Mouton) isolator that employed laser annealing on a large scale to eliminate the growth-induced anisotropy which caused the magnetization of garnet films to lie out of the plane.

Forward traveling wave

H_0

45°

Optically active rotation

Magneto-optic rotation

Backward traveling wave

H_0

45°

Optically active rotation

Magneto-optic rotation
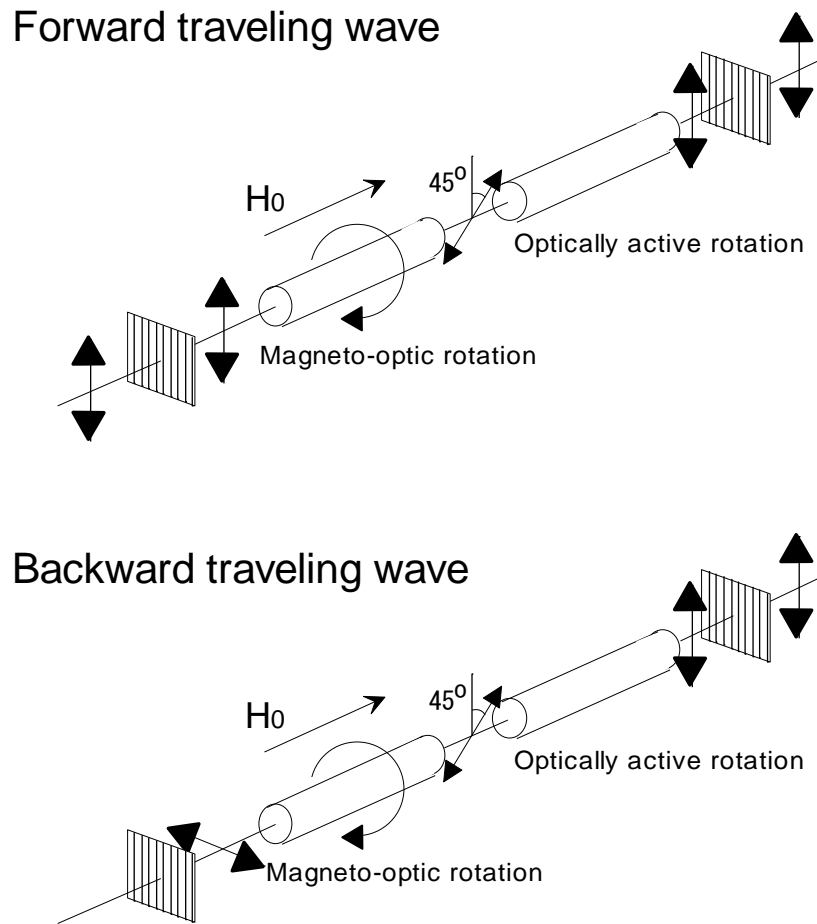
Figure 1.3 Operation principle of an optical isolator with parallel polarizers.

Mode selector

Substrate

Mode selector

Magneto-optic layer

Optically active or anisotropic crystal
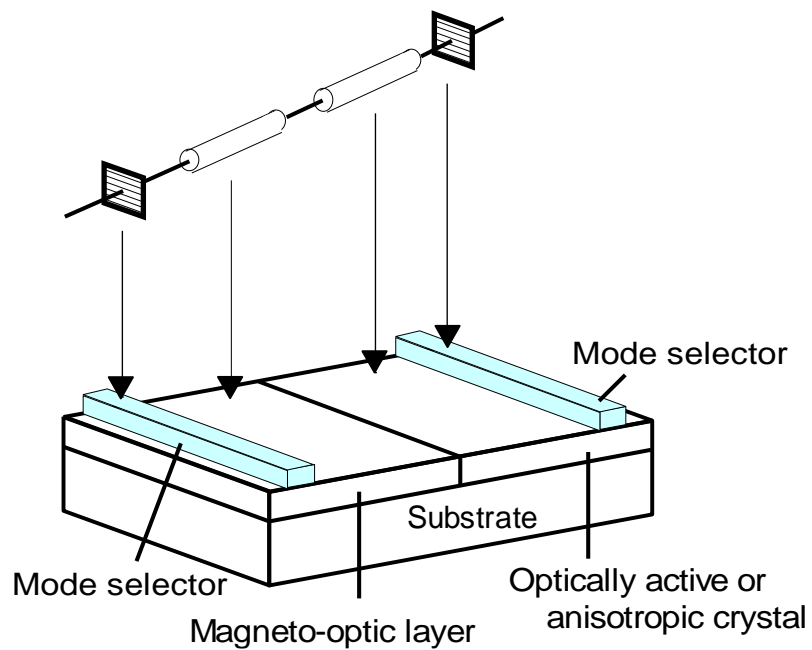
Figure 1.4 The structure of waveguide-type optical isolator employing mode conversion.
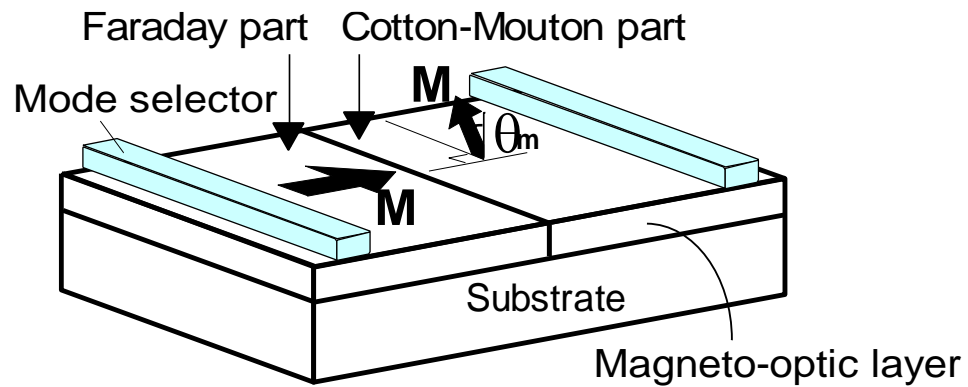
Figure 1.5 The diagram of mode-conversion isolator.

Another type of the waveguide-type isolator is a "semileaky isolator". An anisotropy was realized within refractive indices that were higher or lower than the garnet waveguide in order to obtain "semi-leaky" waveguides [29]. Figure 1.6 shows the basic geometry of the semileaky optical isolator. The nonreciprocal magneto-optic mode conversion was designed to be equal but opposite in the forward direction, then TE mode would experience little loss. On the other hand, in the backward direction, TM modes were generated and leaked away due to the higher cladding index. Due to the problem in an optical contact between the magneto-optic guiding layer and anisotropic superstrate, it is very difficult to fabricate this isolator [30].
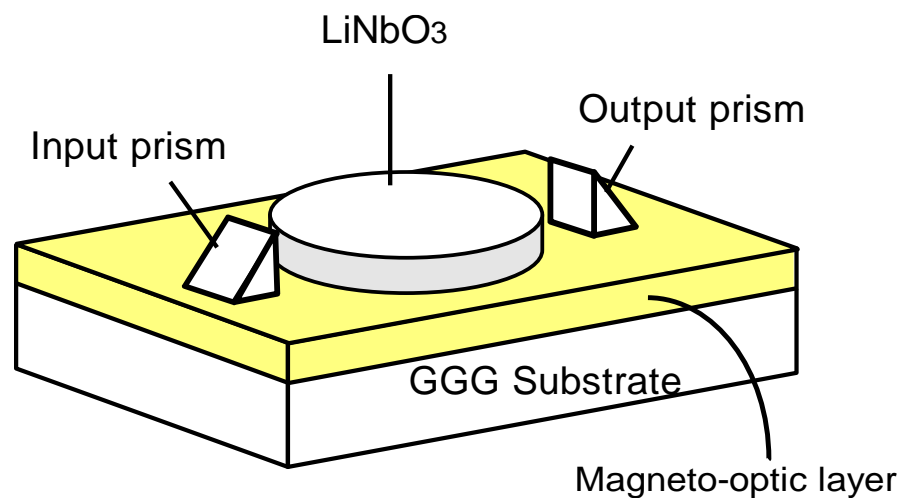
Figure 1.6 Basic geometry of the semileaky optical isolator.

An optical isolator employing a nonreciprocal phase shift is attractive because there is no need for phase matching or complicated control of the direction of magnetization [31]. The nonreciprocal phase shift occurs in TM modes travelling in magneto-optic waveguides, in which the magnetization is aligned transversely to the light propagation direction in the film plane. When a magneto-optic layer is used as a cladding layer in the magneto-optic waveguide, the nonreciprocal phase shift has its maximum with a high-refractive-index guiding layer [32].

An optical isolator based on a nonreciprocal guided-radiation mode conversion is realized [33-35]. The isolator operates on the basis of the nonreciprocal guided-radiation mode conversion in a channel waveguide. The optical isolator employing the nonreciprocal guided-radiation mode conversion is very attractive because of its simple structure. A backward TM mode is converted to TE radiation mode while a forward TM mode propagates with no mode conversion by arranging the propagation constant relationship of the two modes. It can be accomplished by the optical nonreciprocal phase shift which occurs in TM modes [36,37].

1.2.3 Optical circulator

Another type of passive element that is commonly used in fiber optic systems is the optical circulator [23,38]. An optical circulator is a special fiber-optic component that can be used to separate optical signals that travel in opposite directions in an optical fiber. It can be made with any number of ports. Moreover, if it makes sure the last port does not circulate around the first, the device can be used in systems where this feature is not required. The optical circulators are very versatile devices and may be used in many applications.

Optical circulators are made of an assembly of optical components. There are many different designs but the key principle is like that of the optical isolator. The basic function of an optical circulator is illustrated in the figure 1.7. For example, in a 3-port circulator, a signal is transmitted from port 1 to port 2, another signal is transmitted from port 2 to port 3, and finally, a third signal can be transmitted from port 3 to port 1. In terms of operation principles, optical circulators can be divided into three types, traditional, waveguide, and holographic. The traditional optical circulators consist of spatial walk-off polarizers (SWPs), Faraday rotators (FRs), and half-wave plates (Hs) to implement its function. [39]
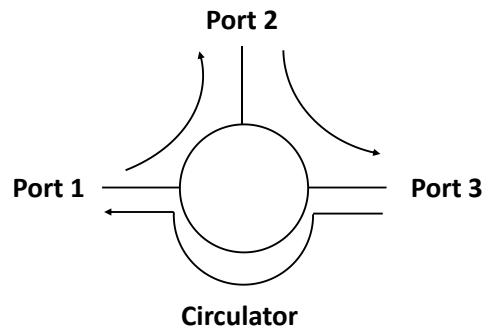
Figure 1.7 Behavior of an optical circulator.

1.3 Si photonics

For the global market of Si photonics, the Si photonics market is estimated to be USD 774.1 million in 2018 and is expected to USD 2.61 billion in 2024 that means the compound annual growth rate (CAGR) is growing up to 22.45%. This market is reported base on the product, applications, components, and regions. The Si photonics is produced for a transceiver, a switch, a variable optical attenuator, a cable, and a sensor. The Si photonics is realized in the application such as data center, telecommunications, military and defense, medical and life sciences, and sensing. The Si photonics is a perfect solution for high-density photonic integration, allowing the incorporation of photonic devices on a Si wafer. The problem to transfer huge data should be resolved through high-density photonic integration with photonics devices.

Si photonics means the implementation of some level of photonic integrated circuit in Si. The emergence of photonics and electronics based on a Si platform creates an ideal solution for optoelectronic integrated circuit which potentially enables optical interconnects with power consumption [40]. More than a decade's researches, Si-based photonic devices are rapidly increasing their performances. Si-based micro and nano-waveguide devices have shown a lot of advantages, including high speed [41], low optical loss [42], low power consumption [43], small size [44], monolithic optoelectronic integrations [45], and hybrid material integration capability [46]. Si photonics has been developed as an integration technology that supports a wide range of compact photonic device on an integrated circuit for applications ranging from communication to sensing. Si photonics is employed in the project of HELIOS, PLATON, ePIXnet, iPHOS, RAMPLAS, PARADIGM, etc. [47]

For example, HELIOS proposes to integrate Si photonic components with integrated circuits. HELIOS intends to realize a design and fabrication chain for integrating the photonic layer with CMOS circuit by using microelectronic fabrication processes. [48] HELIOS aims to develop a generic integration and manufacturing technology for high density and high-performance components and circuits involving passive and active photonic functions.

PLATON [49, 50] purposes to develop and demonstrate on-chip Tb/s optical router for back-plane or blade-server interconnects through merging plasmonics and silicon photonics technology, employing plasmonics for the switching functionalities and silicon photonics for filtering, multiplexing, and header detection processes. PLATON includes a router-chip with integrated photonics, plasmonics, and microelectronic components. PLATON aims to reduce the size and power consumption bottleneck in data center and high-performance computing system by realizing chip-scale high-throughput routing fabric with reduced energy consumption and footprint requirement. PLATON's optical board technology is used to blend the functionally potential small-footprint, high-bandwidth plasmonic structures and the potential integration of plasmonics with the more mature silicon-on-insulator (SOI) technology providing a new generation of miniaturized photonic components.

Si is used as an optical medium and in complementary metal-oxide semiconductor fabrication processing technology. It allows tighter monolithic integration of many optical functions with a single device. Optical waveguides, modulators, and photo-detectors can be integrated within a single device, thus providing a smaller form factor. Many existing devices still require external laser sources and, therefore, light coupling capabilities at the input and output of a Si photonics IC are critical to the success of the product. There are still numerous challenges designers need to overcome in order to make Si photonics devices viable for mass adoption and the technology of choice for future optoelectronic communication. In 2015, Si photonics fundamentals were presented, the basic building blocks covering both active and passive elements, and discuss the contrast with existing multimode/single mode optoelectronics technology. It will provide an overview of the challenges which designers have already conquered to bring this technology to a stage where successful products are demonstrated.

Si photonics has attracted attention as an emerging technology for optical telecommunications and for optical interconnects in microelectronics. Based on complicated semiconductor technology, Si photonics would be provided with and inexpensive integrated electronic-photonic platform. For the silica-based or III-V semiconductor-based photonic systems, Si photonics requires an optical waveguide system. The III–V compound semiconductor-based waveguides and photonic devices have geometries

smaller than those in the silica-based system; however, on a Si substrate it is very difficult to grow epitaxially the high-quality III–V materials needed for the construction of practical photonic devices.

Moreover, Si waveguides, such as rib-type waveguides with core dimensions of a few micrometers [51] and photonic wire waveguides with core dimensions of several hundreds of nanometers [52–54], are considered. The waveguide must have features that allow accommodating passive and dynamic photonic devices such as wavelength filters and modulators. The waveguide system must be flexible enough to allow active functions, such as light emission and detection to be implemented. A Si-based waveguide is obviously preferable for electronic photonic convergence.

1.4 Waveguide optical isolator for Si photonics

As for the communication network, the fiber optic supports the coming multimedia based society. This system is indispensable for transmitting audio data, as has been conventionally performed, in addition to transmitting large-volume data such as move data freely. The reflection of the bifurcation of optical fiber causes amplifier or laser diode failure, it has become a problem alongside the widening of services. Recently, branch connection systems for high-speed transmission or for a large number of subscribers, various other optical parts are required in addition to these core parts. These include optical amplifiers, splitters, optical isolators, optical couplers, optical branching filters, optical switches, optical modulators, optical attenuators, etc. Generally, the laser diode of the optical transmitter is built in the laser diode module integrated with optical parts such as the optical fiber. The optical isolator is located between the laser diode and the optical fiber and prevents the penetration of reflected light to the laser diode.

An optical isolator is essential for protecting the active photonic devices from unwanted refracted light. In decade ago, the optical isolators with a Si guiding layer have been widely researched and lead to the optical isolator design. In order to increase transmit capacity, the light source should have a high-coherence operation and therefore becomes sensitive to optical feedback. A bulk-type optical isolator is installed using laser sub mount in a silicon transceiver chip based on CMOS photonics technology. Therefore, an optical isolator on a silicon platform is required. H. Yokoi, et al. proposed the optical isolator in Mach-Zehnder interferometer (MZI) devices with a Si guiding layer that was integrated in a garnet cladding on SOI [55] as shown in figure 1.8. The optical isolators have been developed and

operated on the magneto-optic phenomenon of a nonreciprocal phase shift, rather that polarization conversion as for Faraday rotation based isolators [56]. As for MZI structure, there are complex waveguides. These structures need to apply the external magnetic field in two directions for isolator operation.
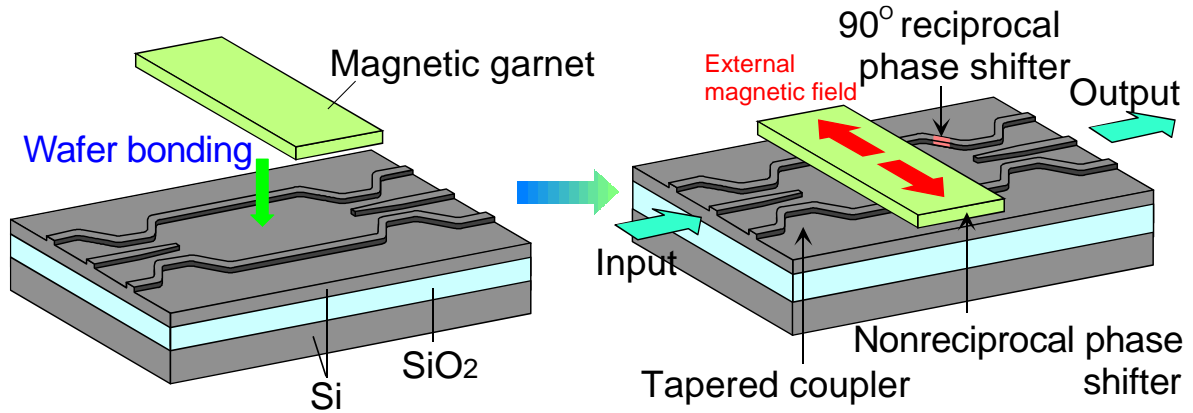
Figure 1.8 The schematic drawing of SOI waveguide MZI optical isolator.

At the present, the author proposes rib-type optical isolators with the Si guiding layer. The rib-type waveguide is a simple structure. The external magnetic field is applied in these structure in one direction for isolator operation. The magneto-optic waveguide on the SOI substrate can be fabricated by bonding technique [57,58]. In the magneto-optic waveguide, the Si guiding layer is deposited on the SiO_2 as shown in figure 1.9. In this research, the author focuses on surface activated bonding and photosensitive adhesive bonding since they are suitable for bonding between Si and magnetic garnet at low temperature.
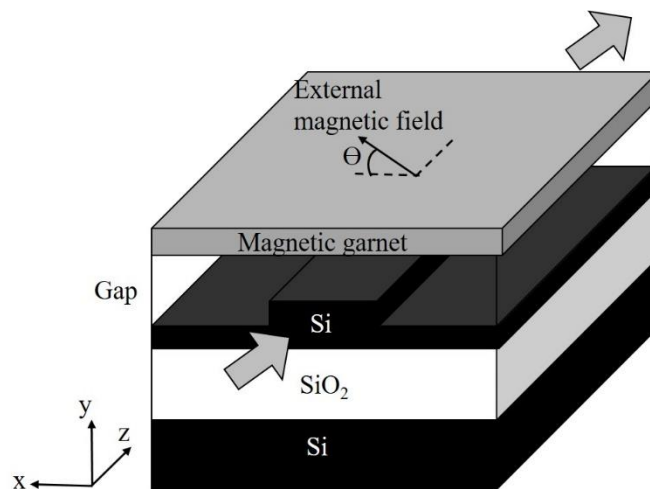
Figure 1.9 Optical isolator with Si guiding layer fabricated by bonding technique.

H. Yokoi et al. have proposed an optical isolator with a Si guiding layer deposited on a magnetic garnet layer [59]. Recently, an amorphous Si has attracted attention for integrated optics because of its low absorption loss and high refractive index [60-62]. In this thesis, the optical isolator with a hydrogenated amorphous Si (a-Si:H) guiding layer deposited on a garnet substrate is considered. The optical isolator with an a-Si:H guiding layer is shown in figure 1.10. The optical isolator employing the nonreciprocal guided-radiation mode conversion is designed. The principle of the nonreciprocal phase shift will be explained in the next chapter.
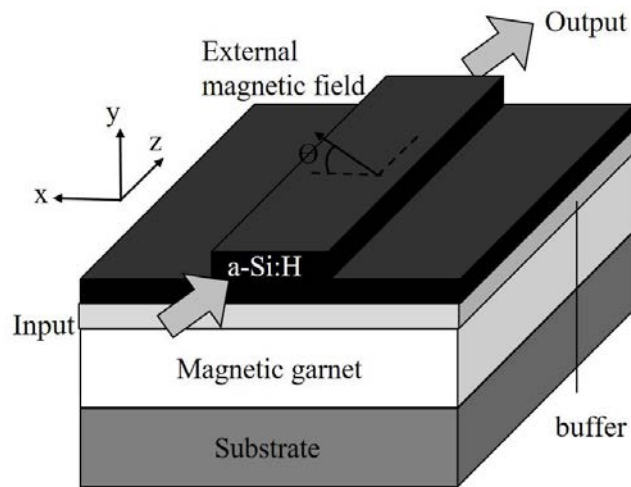
Figure 1.10 Optical isolator with hydrogenated amorphous Si (a-Si:H) guiding layer deposited on a magnetic garnet cladding layer.

From above, there are several types of a magneto-optic waveguide for optical isolators. The advantages and disadvantages of each waveguide type are considered as shown in table 1.1.

Table 1.1 The advantages and disadvantages of the magneto-optic waveguide for optical isolators.

Optical isolator type	Advantage	Disadvantage
Mode conversion isolator	- Low loss - Easy to be aligned magneti-zation on a film plane.	- Need phase matching between TE and TM modes
Semileaky optical isolator	- Large fabrication tolerance - Wide operating wavelength range	- Need phase matching between TE and TM modes - Difficult to fabricate
MZI optical isolator	- No need for phase matching between TE and TM modes	- complex waveguide - Need the external magnetic field in two direction.
Rib-type optical isolator	- No need for phase matching between TE and TM modes - Use a simple structure. - Apply the external magnetic field in one direction.	- Difficult of deposited the Si on magnetic garnet.

1.5 Organization of the dissertation

The optical fiber communication is used to transmit light and information over long distances. The optical isolator is indispensable in protecting optical active devices from unwanted reflected light. The waveguide optical isolator is desired in order to realize a photonic integrated circuit. In the near-infrared region, magnetic garnet crystals are necessary components for an optical nonreciprocal device because of their transparency and strong magneto-optic effect. Developing Si photonics technology, optical isolators with the Si guiding layer are desired.

This dissertation is composed of six chapters.

In chapter 1 "introduction", the background of the optical fiber communication is introduced. The optical nonreciprocal devices are classified in a bulk optical isolator, waveguide optical isolators, and an optical circulator. Si photonics and a waveguide optical isolator for Si photonics are also introduced.

In chapter 2 "theories", this chapter will explain propagation of light wave in the waveguide. The properties of garnet materials for optical isolators will be clarified. The magneto-optic effect is classified in Faraday effect, Cotton-Mouton effect, and Kerr effect. The calculation of the nonreciprocal phase shift will be described by solving the Maxwell equation. Moreover, the theory of fabrication process of magneto-optic waveguides is also illustrated such as surface activated bonding, photosensitive adhesive bonding, plasma-enhanced chemical vapor deposition (PECVD), spin coating, electron beam lithography (EBL), ultraviolet lithography, and etching.

In chapter 3 "magneto-optic waveguides fabricated by bonding technique", the optical isolator employing the nonreciprocal phase shift is designed. An optical isolator constructed on a SOI substrate, a widely adopted substrate for modern optical devices is explained. The magneto-optic waveguide on the SOI substrate can be fabricated by bonding technique. An optical isolator employing a nonreciprocal guided-radiation mode conversion consists of a rib-type magneto-optic waveguide with a Si guiding layer. The optical isolator employing the nonreciprocal guided-radiation mode conversion is realized by calculating the isolation ratio. The electric field of TM guided mode and TE radiation mode are studied. Design of the optical isolator fabricated by surface activated bonding or photosensitive adhesive bonding is considered. Relationship of waveguide parameters for isolator operation is clarified for various gaps.

In chapter 4 "magneto-optic waveguides with a-Si:H guiding layer", an optical isolator with the amorphous Si guiding layer on a garnet substrate is investigated. The relationship of rib height and rib width for the isolator operation is clarified. The optical isolator employing the nonreciprocal guided-radiation mode conversion is realized by calculating the isolation ratio. The electric field of TM guided mode and TE radiation mode are studied. The magneto-optic waveguide with the a-Si:H guiding layer is fabricated and evaluated.

In chapter 5 "athermal operation of optical isolator", the temperature dependence of the optical isolator is investigated. The relationship of rib height and rib width for the isolator operation is clarified for various operating temperatures. Refractive indices of layers in a magneto-optic waveguide are considered to circumvent the deviation of the waveguide parameters for isolator operation due to the temperature shift.

Finally, conclusions and recommendation are presented in chapter 6.

References

[1] T. H. Maiman, 1960, "**Optical and Microwave-Optical Experiments in Ruby**," Phys. Rev. Letters, Vol. 4, No. 11, pp.564-566.

[2] https://lemelson.mit.edu/resources/robert-hall

[3] I. Hayashi, M. B. Panish, P. W. Foy, and S. Sunski, 1970, "**Junction Lasers Which Operate Continuously at Room Temperature**," Appl. Phys. Lett. 17, p. 109.

[4] K. Mettler, 1987, "**Design and Performance of High Power Semiconductor Lasers**," Solid State Device Research Conference, European, pp. 817-825.

[5] F. S. Choa, T. L. Koch, U. Koren, and B. I. Miller, 1989, "**Optoelectronic Properties of InGaAs/InGaAsP Multiplr-quantum-well Waveguide Detectors**," IEEE photon. Technol. Lett., Vol. 1, pp. 376-378.

[6] K. C. Kao, and G. A. Hockham, 1966, "**Dielectric-fibre surface waveguides for optical frequencies**," IEEE Proc. Vol. 113, pp. 1151-1158.

[7] F. P. Kapron, D.B. Keck, and R. D. Maurer, 1970, "**Radiation Losses in Glass Optical Waveguides**," Appl. Pyhs. Lett., Vol. 17, p.423.

[8] R. G. Smith, 1972, "**Optical Power Handling Capacity of Low Loss Optical Fibers as Determined by Stimulated Raman and Brillouin Scattering**," Appl. Opt., Vol. 11, No. 11, pp. 2489-2494.

[9] S. E. Miller, 1969, "**Integrated optics: An Introduction**," Bell Syst. Tech. J., Vol. 48, p. 2059.

[10] W. S. C. Chang, M. W. Muller, and F. J. Rosenbaum, 1974, "**Integrated Optics**," Laser Appl. (Academic, New York), Vol. 2, p.1867.

[11] H. Kogelnik, 1975, "**An Introduction to Integrated Optics**," IEEE Trans. Microwave Theory Tech., Vol. 23, p. 2.

[12] Y. Suematsu, 1975, "**The progress of Integrated Optics in Japan**," IEEE Trans, Microwave Theory Tech., Vol. 23, p. 16.91978

[13] C. P. Lee, S. Margalit, I. Ury, and A. Yariv, 1978, "**Integration of an injection laser with a Gunn oscillator on a semi-insulating GaAs substrate**," Appl. Phys. Lett., Vol. 32, pp. 806-807.

[14] J. J. Hsieh, 1976, "**Room- temperature Operation of GaInAsP/InP Double Heterostructure Diode Lasers Emitting at 1.1 um**," Appl. Phys. Lett., Vol.28, p.283.

[15] T. L. Koch., F. S, Choa, U. Koren, R. P. Gnall, F. Hemandez-Gill, C. A. Burrus, M. G. Young, M. Oron, and B. I. Miller, 1990, "**Balanced operation of a GaInAs/GaInAsP multiple-quantum-well integrated heterodyne receiver**," IEEE Photon. Tech. Lett., Vol. 2, pp. 577-581.

[16] R. Lang, and K. Kobayashi, 1980, "**External Optical Feedback Effects on Semiconductor Injection Laser Properties**," IEEE J. of Quantum., Vol. QE-16, pp. 347-355.

[17] Y.-T. Sheen, 2007, "**An Analysis Method for the Vibration Signal with Amplitude Modulation in a Bearing System**," J. of Sound and Vibration, Vol. 303, pp. 538-552.

[18] H. Fukui, K. Furuya, and Y. Suematsu, 1987, "**Suppression of mode hopping noise caused by external reflaction in dynamic single mode (DSM) laser**," Trans. IEICEv Vol. E70, No. 7, pp. 857-864.

[19] K. Ikeda, and O. Akimoto, 1982, "**Instability leading to periodic and chaotic self-pulsatations in a bistable optical cavity**," Phys. Rev. Lett., Vol. 48, pp. 617-620.

[20] S. Yanase, R. N. Mondal, Y. Kaga, and K. Yamamoto, 2005, "**Transition from Steady to Chaotic States of Isothermal and Non-isotermal Flows through a Curved Rectangular Duct**," J. of the Physical Society of Japan, Vol. 74, No. 1, pp. 345-358.

[21] D. Lenstra, B. H. Verbeek, and A. J. den Boef, 1985, "**Coherence collapse in single-mode semiconductor lasers due to optical feedback**," IEEE J. Quant. Electron., Vol. OE-21, pp. 674-679.

[22] Ki Young Kim, 2010, "**Advances in Optical Photonic Devices**," 1st ed., In Tech, Shanghai, China, pp.117 - 135.

[23] http://www.fiber-optic-equipment.com/the-working-principle-of-the-optical-circulator.html.

[24] K. Chang, and W. Sorin, 1990, "**High-performance single-mode fiber polarization-independent isolators**," Opt. Lett., Vol. 15, Issue 8, pp. 449 - 451.

[25] K. Nakajima, Y. Numajiri, and Y. Nomi, 1991, "**New design of a polarization-independent optical isolator with high performance,**" IEEE Trans. Magn., Vol. 27, Issue 6, pp. 5399 -5401.

[26] T. Matsumoto, 1979, "**Polarization-Independent Isolators for Fiber Optics**," Trans. IECE Japan, E62, pp. 516-517.

[27] J. P. Castera, and G. Hepner, 1997, "**Isolator in integrated optics using the Faraday and Cotton-Mouton effects**," IEEE Trans. Magn. MAG-13, pp. 1583-1585.

[28] K. Ando, T. Okoshi, and N. Koshizuka, 1988, "**Waveguide magneto-optic isolator fabricated by laser annealing**," Appl. Phys. Lett., Vol. 53, No. 1, pp. 4-6.

[29] S. T. Kirsch, W. A. Biolsi, S. L. Blank, P. K. Tien, R. J. Martin, P. M. Bridenbaugh, and P. Grabbe, 1981, "**Semi-leaky thin film optical isolator**," J. Appl. Phys., Vol. 52, no. 5, pp. 3190 -3199.

[30] S. Yamamoto, Y. Okamura, and T. Makimoto, 1976, "**Analysis and design of semileaky-type thin-film optical waveguide isolator**," IEEE J. Quantum Electron., Vol. QE-12, pp. 764-770.

[31] H. Yokoi, T. Mizumoto, T. Takano, and N. Shinji, 1990, "**Demonstration of an optical isolator by use of a nonreciprocal phase shift**," Appl. Opt., Vol. 38, pp. 7409-7413.

[32] H. Yokoi, 2008, "**Calculation of nonreciprocal phase shift in magneto-optic waveguides with Ce: YIG layer**," Opt. Mater., Vol. 31, pp. 189-192.

[33] T. Shintaku and T. Uno, 1994, "**Optical waveguide isolator based on non- reciprocal radiation**," J. Appl. Phys. Vol 76, no. 12, pp. 8155 - 8159.

[34] T. Shintaku, 1995, "**Integrated optical isolator based on nonreciprocal higher- order mode conversion**," Appl. Phys. Lett. Vol. 66, no. 21, pp. 2789 - 2791.

[35] T. Shintaku, 1998, "**Integrated optical isolator based on efficient nonreciprocal radiation monde conversion**," Appl. Phys. Lett. Vol. 73, no. 14, pp. 1946 - 1948.

[36] S. Yamamoto, and T. Makimoto, 1974, "**Circuit theory for a class of anisotropic and gyrotropic thin-film optical waveguides and design of nonreciprocal devices for integrated optics**," J. Appl. Phys., Vol. 45, pp. 882-888.

[37] F. Auracher, and H. H. Witte, 1975, "**A new design for an integrated optical isolator**," Optics Commun., Vol. 13, pp. 435-438.

[38] http://www.fiberopticshare.com/passive-optical-components-optical-circulator.html.

[39] F.-H. Hsu, J.-H. Chen, K.-H. Chen, C.-H. Yeh, and K. Y. Hsu, 2014, "**Optimized design of multiport optical circulator**," Optik, Vol. 125, pp. 2454-2457.

[40] D. A. B. Miller, 2009, "**Device requirements for optical interconnects to silicon chip**," Proc. IEEE, Vol. 97, pp. 1166-1185.

[41] L. Vivien, A. Polzer, D. Marris-Morini, J.-M. Hartmann, P. Croza, E. Cassan, C. Baudot, F. Boeuf, and J.-M. Fedeli, 2013, "**40 Gbit/s germanium waveguide photodiode,**" Opt. Express, Vol. 20, pp. 1096-1101.

[42] G. Li, J. Yao, H. Thacker, A. Mekis, X. Zheng, I. Shubin, Y. Lo, J.-H. Lee, K. Raj, J. E. Cunningham, and A. V. Krishnamoorthy, 2012, "**Ultralw-loss, high-density SOI optical waveguide routing for macrochip interconnects**," Opt. Express, Vol. 20, pp.12035-10239.

[43] W. A. Zortman, A. L. Lentine, D. C. Trootter, and M. R. Watts, 2011, "**Low-voltage differentially-signaled modulators**,", Opt Express, Vol.19, pp. 26017-26026.

[44] Q. Xu, D. Fattal, R. G. Beausoleil, 2008, "**Silicon microring resonators with 1.5-μm radius**," Opt. Express, Vol. 16, pp.4309-4315.

[45] C. Gunn, 2006, "**CMOS photonics for high-speed interconnects**," IEEE Micro., Vol. 26, pp. 58-66.

[46] D. Liang, G. Roelkens, R. Baets, and J. E. Bowers, 2010, "**Hybrid Integrated Platforms for Silicon Photonics**," Materials, Vol. 3, pp. 1782-1802.

[47] http://www.semicontaiwan.org/en/sites/semicontaiwan.org/files/data16/docs/(7)%20SEMICON%20Tai wan%202016_Tekin_05.pdf.

[48] J. M. Fedeli, L. Di Cioccio, D. Marris-Morini, L. Vivien, R. Orobtchouk, P. Rojo-Romeo, C. Seassal, and F. Mandorlo, 2008, "Development of Silicon Photonics Devices Using Microelectronic Tools for the Integration on Top of a CMOS Wafer," Advances in Opt. Tech. AOT, special issue: Silicon Photonics, Article ID 412518.

[49] S. Papaioannou, K. Vyrsokinos, D. Kalavrouziotis, G. Giannoulis, D. Apostolopoulos, H. Avramopoulos, F. Zacharatos, K. Hassan, J. – C. Weeber, L. Markey, A. Dereux, A. Kumar, S. I. Bozhevolnyi, A. Suna, O. G. de Villasante, T. Tekin, M. Waldow, O. Tsilipakos, A. Pitilakis, E. E. Kriezis, and N. Pleros, 2012, "Merging Plasmonics and Silicon Photonics Towards Greener and Faster "Network-on-Chip" Solutions for Data Centers and High-Performance Computing Systems," INTECH, chap. 21, pp. 523-548.

[50] M. Humer, R. Guider, W. Jantsch, and T. Fromherz, 2013, "Integration, photostability and spontaneous emission rate enhancement of colloidal PbS nanocrystals for Si-based photonics at telecom wavelengths," OSA. Ppt. Express, Vol. 21, No. 16, pp. 18680-18688.

[51] A.G. Rickman, G.T. Reed, and F. Namavar, 1994, "**Silicon-on-insulator optical rib waveguide loss and mode characteristics**," J. Lightwave Tech., Vol. 12, pp. 1771–1776.

[52] K. Yamada, T. Tsuchizawa, T. Watanabe, J. Takahashi, E. Tamechika, M. Takahashi, S. Uchiyama, H. Fukuda, T. Shoji, S. Itabashi, and H. Morita, 2004, "**Microphotonics devices based on silicon wire waveguiding system**," IEICE Trans. Electron., Vol. E87-C, pp. 351–358.

[53] T. Tsuchizawa, K. Yamada, H. Fukuda, T. Watanabe, J. Takahashi, M. Takahashi, T. Shoji, E. Tamechika, S. Itabashi, and H. Morita, 2005, "**Microphotonics devices based on silicon microfabrication technology**," IEEE J. Sel. Top. Quantum. Electron., Vol. 11, pp. 232–240.

[54] P. Dumon, W. Bogaerts, V. Wiaux, J. Wouters, S. Beckx, J. V. Campenhout, D. Taillaert, B. Luyssaert, P. Bienstman, D. V. Thourhout, and R. Baets, 2004, "**Low-loss SOI photonic wires and ring resonators fabricated with deep UV lithography**," Photon. Technol. Lett., Vol. 16, 1328–1330.

[55] H. Yokoi, T. Mizumoto, and Y. Shoji, 2003, "**Optical nonreciprocal devices with a silicon guiding layer fabricated by wafer bonding,**" Appl. Opt., Vol. 42, No. 33, pp. 6605-6612.

[56] Y. Shoji, I. W. Hsieh, R. M. Osgood, and T. Mizumoto, 2007, "**Polarization-Independent Magneto-Optical Waveguide Isolator Using TM-Mode Nonreciprocal Phase Shift**," J. Lightwave Technol. Vol. 25, pp. 3108 - 3113.

[57] T. Mizumoto, and Y. Shoji, 2014, "**Optical Isolators and Circulators on Si Waveguide Platforms,**" Int. Conf. on Solid State Devices and Mater., pp. 502-503.

[58] C.-T. Ko, and K.-N. Chen, 2012, "**Low Temperature bonding technology for 3D integration,**" J. Microelectron. Reliability, Vol. 52, Issue 2, pp. 302-311.

[59] H. Yokoi, K. Sasaki, and T. Aiba, 2009, "**Sputter-deposited Si layer for optical isolator with Si guiding layer**," Jpn. J. Appl. Phys., Vol. 48, pp. 062202-1-062202-4.

[60] G. Cocorullo, F. G. D. Corte, R. De Rosa, I. Rendina, A. Rubino, and E. Terzini, 1998, "**Amorphous silicon-based guided-wave passive and active devices for silicon integrated optoelectronics**," IEEE J. Sel. Top. Quantum Electron., Vol. 4, No. 6, pp. 997-1002.

[61] A. Harke, T. Lipka, J. Amthor, O. Horn, M. Krause, and J. Miller, 2008, "**Amorphous silicon 3-D tapers for Si photonic wires fabricated with shadow masks**," IEEE Photon. Tech. Lett., Vol. 20 pp. 1452-1454.

[62] Y. Shoji, T. Ogasawara, T. Kamei, Y. Sakakibara, S. Suda, K. Kintaka, H. Kawashima, M. Okano, T. Hasama, H. Ishikawa, and M. Mori, 2010, "**Ultrafast nonlinear effects in hydrogenated amorphous silicon wire waveguide**," Opt. Exp., Vol. 17, pp. 5668-5673.

CHAPTER 2 THEORIES

2.1 Propagation of light wave

Light is a part of the electromagnetic spectrum, which is the collection of all waves such as visible light, microwaves, radio waves, and X-rays. In 1665, I. Newton [1,2] believed that light consists of a large number of minute material corpuscles emitted by a luminous body which produces the sensation of sight when these corpuscles strike the eye. The light travels with a tremendous speed in straight lines and homogeneous medium. This theory is used to explain the principle of rectilinear of light, laws of reflection as well as the law of refraction. A wavefront is a surface over which an optical wave has a constant phase. For example, a wavefront can be the surface over which the wave has a maximum or a minimum value. The shape of a wavefront is usually determined by the geometry of the source such as plane waves, cylindrical waves, and spherical waves. The direction of the wave propagation is always perpendicular to the surface of the wavefront at each point. However, the wavesfronts are produced by a point source in which they are concentric spheres in the principle.

In 1678, C. Huygens [3] considered the light waves propagation in longitudinal and explained the phenomenon of reflection, refraction, interference, and diffraction. When a wave travels in a single medium at a constant speed, the Huygen's construction preserves the general form of the wavefront. That is, spheres propagate and become larger spheres, cylinders become larger cylinders, etc. If a portion of the wavefront enters a different medium, then the wavelets generated by each portion of the wavefront travel with the velocity that is appropriate for the medium that the wavefront locates. That is, the wavelets in the medium where the speed of light is lower will have smaller radii than the wavelets in the original medium. Michelson-Morley's [4] experiment failed to detect the presence of ether, therefore, the ether concept was relinquished.

The basic structure of a dielectric waveguide composes of optical medium with high-index (core layer), that will be surrounded around low-index media (cladding layer). When the light wave is propagating along the longitudinal (z) direction, the characteristics of a waveguide are determined in the transverse direction profile of its dielectric constant $\varepsilon(x,y)/\varepsilon_o$, that is independent of the longitudinal (z)

direction. The characteristics of a waveguide depend on the transverse direction profile of the refractive index $n(x,y)$. There are two types of waveguide. First, it is a planar waveguide. There is an optical confinement in only one direction, the core is sandwiched between cladding layers in one direction. The core layer is called film, meanwhile the cladding layer is called cover and substrate, respectively. Second, it is a non-planar waveguide that is two dimensional transverse optical confinement. The core is covered by the cladding layer, and $n(x,y)$ is a function of both x and y coordinates.

The optical waveguides are the important structure in semiconductor lasers used in order to control the light for various distance, and used in both passive and active devices. For waveguide, the index has abrupt changes between core and cladding that is called a step-index waveguide, meanwhile the index profile varying gradually is called a graded-index waveguide. Mostly, non-planar waveguides are used for device applications. The non-planar waveguides have a lot of types, that are differentiated by the distinctive feature of the index profiles. The waveguide types come from the group of non-planar waveguides, which include strip-loaded waveguides, ridge waveguides, rib waveguides, buried channel waveguides, and diffused waveguides as shown in figure 2.1(a)-(e).
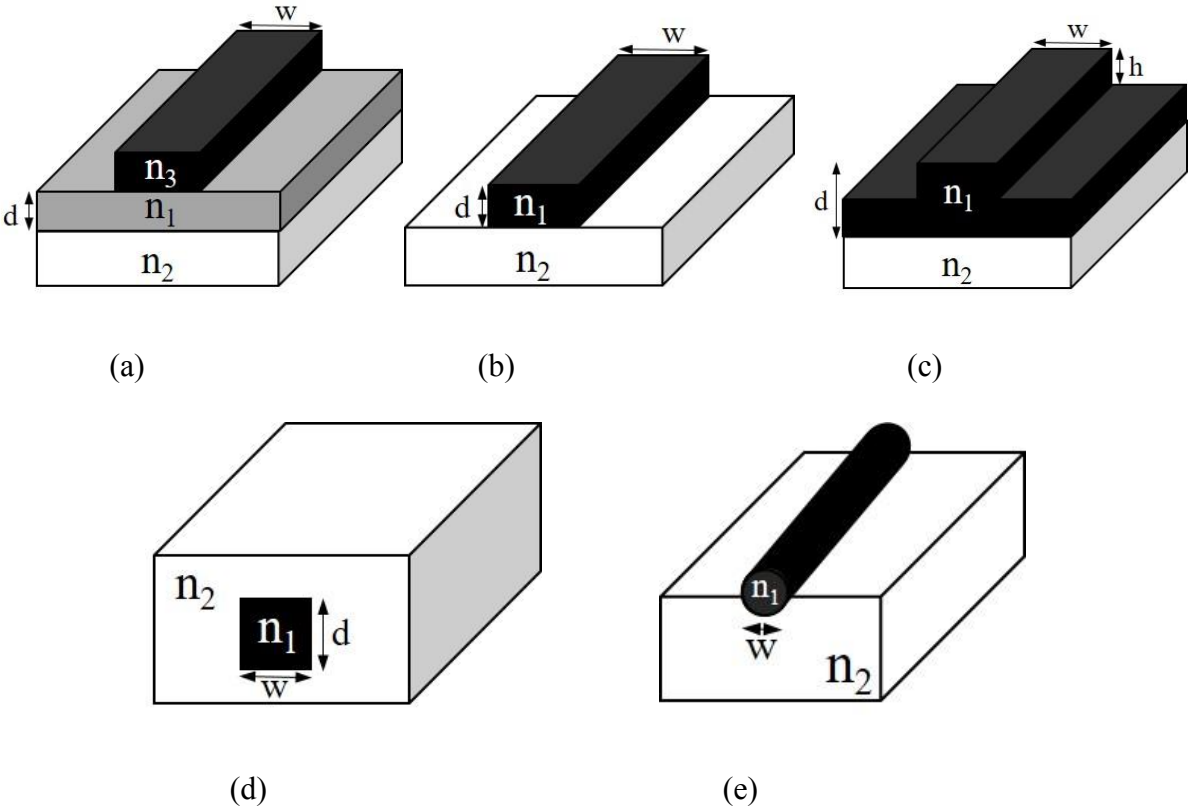
Figure 2.1 Structure of non-planar waveguides, consisting of (a) strip-loaded waveguides, (b) ridge waveguides, (c) rib waveguides, (d) buried channel waveguides, and (e) diffused waveguides.

2.2 Garnet crystal

Garnets are some of the most magnetic gemstones. The most of all of the garnets acquire in the same properties and crystal forms, however, it has different chemical composition. Normally, the general formula of garnet is $X_3Y_2(SiO_4)_3$. The X site is usually occupied by divalent cations (Ca, Mg, Fe, Mn) and the Y site by trivalent cations (Al, Fe, Cr) in an octahedral/ tetrahedral framework with SiO$_4$ occupying the tetrahedral. Most gemologist garnets [5] are based on their color, refractive index, and absorption spectrum [6-8]. Magnetic susceptibility measurements in conjunction with refractive index can be used to distinguish garnet species and varieties, and determine the composition of garnets in terms of percentages of end-member species within an individual gem.

The crystallographic structure of garnet has been expanded with the general formula $X_3Y_2(ZO_4)_3$. For silicon, a large number of element has been instated of Z site including Ge, Ga, Al, V, and Fe [9]. Garnet films have large lattice parameters and thermal expansion mismatch with typical photonic substrates such as Si, GaAs, and InP. Good quality films are made by controlling the deposition and annealing processes. Yttrium iron garnet (YIG), the five iron(III) ions occupy two octahedral and three tetrahedral sites, with the yttrium(III) ions are coordinated by eight oxygen ions in an irregular cube. The iron ions in the two coordination sites exhibit different spins, resulting in magnetic behavior. YIG [10] is a versatile ceramic material with high melting point, large resistivity, high electromagnetic properties, etc. It is well-known as magnetic garnet and widely applied in electronics and microwave communication, such as in isolators, circulators, phase shifters, etc. In addition, Gadolinium Gallium Garnet (GGG) is synthesized for usage as a substrate for liquid-phase epitaxy of magnetic garnet films for bubble memory and magneto-optic applications. In this thesis, a cerium-substituted yttrium iron garnet (Ce:YIG) and calcium-, magnesium-, and zirconium-doped GGG ((Gd,Ca)$_3$(Ga,Mg,Zr)$_5$O$_{12}$ or GCGMZG) were considered.

3.2.1 Cerium-substituted yttrium iron garnet (Ce:YIG)

Optical isolators are realized in the advanced communication systems. Time-reversal symmetry is typically broken using magneto-optic materials whose permittivity tensor has non-vanishing off-diagonal components, such as YIG and Ce:YIG. The waveguide-type magneto-optic devices have many

advantages such as well guided light, low magnetic field requirements, low cost, and the possibility of compact integration. YIG materials have been commercially used in microwave circuits like resonators, isolators, and circulators. There are many researches proposing the YIG waveguides because YIG has a Faraday rotation of several hundreds of deg/cm. Therefore, this order of length is needed for nonreciprocal polarization plane rotation. Large Faraday rotation materials are undesignable for compact integration, and Ce:YIG films have a large Faraday rotation as well. Gomi et al. [11] showed the giant Faraday rotation of Ce:YIG films which has been achieved by using radio frequency sputtering. They focus on the Faraday rotation spectrum and magnetic properties. Moreover, Ce:YIG films have been found to exhibit a large magneto-optic effect and low propagation loss. It will be good candidate material for devices with higher quality [11]. Tate et. al. [12] proposed the crystallinity of Ce:YIG iron garnet film prepared by radio frequency sputtering that was studied by using X-ray diffraction technique and transmission electron microscopy. Ce:YIG iron garnet films were synthesized by conventional radio frequency sputtering with ceramic target. The films were deposited on the substrates of gadolinium gallium garnet (GGG, lattice constant = 12.383Å) and GCGMZG (lattice constant = 12.496Å) [12], meanwhile the Ce:YIG lattice constant is approximately 12.57Å. Therefore, the optical characteristic of Ce:YIG thin films can be grown on the GCGMZG substrate completely.

3.2.2   Gadolinium calcium gallium magnesium zirconium garnet (GCGMZG)

The magnetic garnet single crystal film grown on the substrate is desired to have a large Faraday rotation coefficient to obtain desired magneto-optic effects. In order to form a high quality single crystal film by epitaxial growth, it is required that a lattice constant difference between the substrate and the single crystal to be grown is as small as possible in a temperature range from a film forming temperature to the room temperature. The Faraday rotation coefficient of the magnetic garnet single crystal film remarkably increases by substituting, so that a substrate material used for the film forming is also required to have a larger lattice constant i.e. gadolinium gallium garnet (GGG) added with Ca, Zr, Mg, etc. by obtaining a large lattice constant is used as the single crystal substrate material.

3.3 Magneto-optic effect

The interaction of light is affected by the magnetic state of the medium and involves the electronic structure. The interaction between electromagnetic radiation and magnetically polarized materials results in magneto-optic effects. The important role of these effects of electromagnetism, providing an experimental support to the electromagnetic theory of light, as well as to both classical and quantum theory of matter including the motions of electron spin and spin-orbit coupling. The light is transverse electromagnetic wave which can be linearly, elliptically, or circularly polarized. A polarized light is included as a wave of electric field vector, oscillating along a given direction, and perpendicular to the propagation direction. The phenomena of magneto-optic effect can be explained by Faraday effect, Cotton-Mouton effect, and Kerr effect.

3.3.1 Faraday effect

M. Faraday [13] proposed the polarization of a linearly polarized light beam that is rotated upon propagating through a media which is placed in a magnetic field parallel to the propagation direction as shown in figure 2.2. The longitudinal magnetic field in the medium becomes optically active. The simple form of rotation ($\emptyset$) is proportional to the strength of the magnetic field (B) and the length of the structure (l) as shown in Eq. 1.

$$\emptyset = V \int_0^l B \, dl = VlB \tag{1}$$

V is noted as the Verdet constant that depends on the properties of medium, the ambient temperature, and the wavelength of the incident light [14]. The angle of the rotation depends on the applied magnetic field. V is positive when the magnetic field is generated by positive current.

Figure 2.2 Operation principle of Faraday effect.

The electromagnetic wave in the medium are considered by Maxwell's equation as follow:

$$\nabla . \vec{D} = 0 \tag{2}$$

$$\nabla . \vec{B} = 0 \tag{3}$$

v

l

$$\nabla \times \overrightarrow{H'} = \frac{1}{c}\frac{d\overrightarrow{D}}{dt} \tag{4}$$

$$\nabla \times \overrightarrow{E'} = -\frac{1}{c}\frac{d\overrightarrow{B}}{dt} \tag{5}$$

where $\overrightarrow{D}$ is the electric displacement, $\overrightarrow{B}$ is the magnetic induction, $\overrightarrow{H'}$ is the macroscopic magnetic field, and $\overrightarrow{E'}$ is the electric field. The electric displacement and the magnetic induction are related with the electric ($\vec{\mu}$) and magnetic ($\vec{m}$) moments. They are induced by the electromagnetic wave as follow:

$$\overrightarrow{D} = \overrightarrow{E} + 4\pi \sum_a N_a \overrightarrow{m^a} \tag{6}$$

$$\overrightarrow{B} = \overrightarrow{H} + 4\pi \sum_a N_a \overrightarrow{\mu^a} \tag{7}$$

where N_a is the number of molecules per unit volume in state a. For the first component, the complex induced moment vectors are shown:

$$m_x = \alpha_{xy}E'_y + \beta_{xy}H'_y \tag{8}$$

$$\mu_x = \gamma_{xy}E'_y + \chi_{xy}H'_y \tag{9}$$

where α and χ are the electric and magnetic polarizability tensors, respectively. There are also complex functions of the external magnetic field $\overrightarrow{H}$. The polarizability tensors can be explained:

$$\alpha_{xy} = \alpha_{xy}^{(0)} + \alpha_{xy}^{(1)}E_z + \cdots \tag{10}$$

$$\chi_{xy} = \chi_{xy}^{(0)} + \chi_{xyz}^{(1)}H_z + \cdots \tag{11}$$

The electric and magnetic moments can be explained:

$$\overrightarrow{m} = \alpha_{(0)}\overrightarrow{E'} + \beta_{(0)}\overrightarrow{H'} + \alpha_{(1)}\left(\overrightarrow{E'}x\overrightarrow{H}\right) + \beta_{(1)}\left(\overrightarrow{H'}x\overrightarrow{H}\right) \tag{12}$$

$$\vec{\mu} = \gamma_{(0)}\overrightarrow{E'} + \chi_{(0)}\overrightarrow{H'} + \gamma_{(1)}\left(\overrightarrow{E'}x\overrightarrow{H}\right) + \chi_{(1)}\left(\overrightarrow{H'}x\overrightarrow{H}\right) \tag{13}$$

A complex index of refraction $\widetilde{n_\pm}$ is solved by Maxwell's equation:

$$\widetilde{n_\pm} = 1 + 2\pi \sum_a N_a \{\alpha_{(0)}^a + \chi_{(0)}{}^a \mp i\beta_{(0)}^a \pm i\gamma_{(0)}^a [\pm i\alpha_{(1)}^a + i\chi_{(1)}^a + \beta_{(1)}^a - \gamma_{(1)}^a]H_z\} \tag{14}$$

The Faraday rotation is described by this equation: $\phi = \omega(\widetilde{n_-} - \widetilde{n_+})/2c$. Therefore, the Faraday rotation can be written as follow:

$$\widetilde{\Phi} = -\frac{2i\pi\omega}{c}\sum_a N_a \{-\beta_{(0)}^a + \gamma_{(0)}^a + [\alpha_{(1)}^a + \chi_{(1)}^a]H_z\} \tag{15}$$

The part of $\alpha_{(1)}^a$ and $\chi_{(1)}^a$ are proportional to $\overrightarrow{E'}$ and $\overrightarrow{H'}$ of the incident light and responsible for magnetic optical activity when the external magnetic field is biased. For normal condition, $\alpha_{(0)} \gg \beta_{(0)}, \gamma_{(0)}, \chi_{(0)}, \alpha_{(1)}H_z$; and $\alpha_{(1)} \gg \beta_{(1)}, \gamma_{(1)}, \lambda_{(1)}$, the Eq. 14 can be approximated as follow;

$$\tilde{n} = 1 + 2\pi \sum_a N_a \alpha_{(0)}^a \qquad (16)$$

In term of the atomic vector polarizability, the Faraday rotation beam of linearly polarized light in z direction through a medium of length l will be shown as:

$$\Phi = -\frac{2\pi\omega lN}{nc}\alpha_v <I_z> \qquad (17)$$

where n is the index of refraction, N is the density number of atoms, and $<I_z>$ is the average nuclear spin of the atom [15].

3.3.2   Cotton-Mouton effect

The Cotton-Mouton effect is the double refraction (birefringence) of light in a liquid in a magnetic field at direction of light propagation with the right angle. At first, J. Kerr and C. Majorana observed the colloidal solution. After that, A. Cotton and H. Mouton, who are French scientists, studied the detail of this solution. The Cotton-Mouton effect was observed by considering the monochromatic light that is polarized in 45 degrees with the magnetic field direction. It is passed through a transparent isotropic specimen lying between the poles of a strong electromagnetic. The material of the specimen becomes elliptically anisotropic in the magnetic field, and the light becomes elliptically polarized owing to the propagation in the substance. There are two waves, consisting of the ordinary and extraordinary waves, which have different phase velocities. The difference of refractive indices of ordinary beam (n_0) and the extraordinary beam (n_e) are called the double refraction value, it is

$$n_e - n_0 = CH^2\lambda \qquad (18)$$

where C is the Cotton-Mouton constant that depends on the substance, and temperature. H is the magnetic field strength, and λ is the wavelength of the light. The value $n_e - n_0$ has not yet been measured reliably in gases because the effect is very small.

The Cotton-Mouton effect is related with the magnetic phenomena group that includes Zeeman and Faraday effects. The theory of the Cotton-Mouton effect is analogous with the Kerr effect that will be explained later. The study of the Cotton-Mouton effect can inform the molecular structure, the formation of molecular aggregates, and molecular mobility.

3.3.3 Kerr effect

In 1963, an optical electromagnetic field was capable of producing a measurable modification of the dielectric properties, inducing a birefringence effect: the first experimental observation of the optical Kerr effect was reported [16]. The polarization of the refracted wave becomes elliptical and rotation of polarization is proportional to both magnetization and media thickness. The origin of microscopic is based on the spin-orbit interaction and relativistic effects [14]. These effects are greater for material with a particular symmetry that is refracted in the form of the dielectric tensor. Considering the relationship of a polarized monochromatic wave in the visible range, with pulsation ω and wave number k, propagating in the air and incident perpendicularly on a ferromagnetic material, its electric field is $E(t,z)\ \alpha\ e^{-i(\omega t - kz)}$. The electric displacement (D), the magnetization (M), and the magnetic induction (B) are related with the magnetic field (H) as follow:

$$D_i = \varepsilon_{ij}(\omega)E_j \tag{19}$$

$$B_i = \mu_{ij}(\omega)H_j \tag{20}$$

where $\varepsilon, \varepsilon_r, and\ \mu$ are the tentorial permittivity, relative permittivity, and permeability, respectively. The permeability at the optical frequency is close to the vacuum permeability (μ_0) for magnetic and non-magnetic media. The Maxwell equations are used by assuming the medium that is electrically neutral as follow:

$$\nabla x E = -\partial_t B \tag{21}$$

$$\nabla x H = j + \partial_t D \tag{22}$$

The current density (j) takes into account of the conductivity tensor, σ: $j = \sigma E$. Defining an effective permittivity by $\epsilon' = \varepsilon + i\frac{\sigma}{\omega}$, Eq. 2, Eq. 21, and Eq. 22 derives:

$$\frac{1}{\mu_0}\nabla x \partial_t B = \partial_t j + \partial_t^2 D \tag{23}$$

$$-\nabla x \nabla x E = \omega^2 \mu_0 \left(i \frac{\sigma}{\omega} + \varepsilon \right) E \tag{24}$$

$$k^2 E - (k, E) = \frac{\omega^2}{c^2} \varepsilon' E \tag{25}$$

This last equation can be reformulated by using the complex index, $n_i = \frac{c}{\omega} k_i$:

$$\left(n^2 \delta_{ij} - n_i n_j - \varepsilon'_{ij} \right) E_i = 0 \tag{26}$$

The nonzero solution is given by zeros of the determinant of the pre-factor and leads to the Fresnel formula for the calculation of normal modes of propagation.

It is noteworthy that the importance of off-diagonal terms, which are functions of M and are the reasons of the magneto-optic effect. The Eigen modes are found by replacing these eigenvalues in Eq. 26, and then it can be demonstrated that $E_x = \pm i E_y = e^{\pm i \frac{\pi}{2}} E_y$. This means that there are two waves presenting with a circular polarization, propagating with the index n_+ and n_-. The induction is,

$$D_+ = n_+^2 \left(E_x + i E_y \right), D_- = n_-^2 \left(E_x - i E_y \right) \tag{27}$$

Light is elliptical after refraction. Fresnel coefficients $r_{??}$ for s and p of reflected field E_r, are calculated with incident field E_i and the boundary conditions on the interface. s or p denotes polarization when the electric field of light is orthogonal or parallel to the plane of incidence.

$$\begin{pmatrix} E_{r,p} \\ E_{r,s} \end{pmatrix} = \begin{pmatrix} r_{pp} & r_{ps} \\ r_{sp} & r_{ss} \end{pmatrix} \begin{pmatrix} E_{i,p} \\ E_{i,s} \end{pmatrix} \tag{28}$$

The Kerr rotation, θ_{kerr} and Kerr helicity, η_{kerr} for s and p lights for all magneto-optic Kerr effect modes are defined as,

$$\theta_{kerr,s} = Re \left(\frac{r_{ss}}{r_{sp}} \right) \tag{29}$$

$$\eta_{kerr,s} = Im \left(\frac{r_{ss}}{r_{sp}} \right) \tag{30}$$

$$\theta_{kerr,p} = Re \left(\frac{r_{ps}}{r_{pp}} \right) \tag{31}$$

$$\eta_{kerr,p} = Im \left(\frac{r_{ps}}{r_{pp}} \right) \tag{32}$$

3.4 Nonreciprocal phase shift

The nonreciprocal phase shift (NRPS) [17] is used for enhancing magneto-optic effect in waveguides. The NRPS needs to shift the backward resonance spectrum away from the forward peaks as a scale of half maximum bandwidth. The multilayered magneto-optic waveguide system can be derived to calculate the NRPS. NRPS can be calculated by using Maxwell equations. The dimensionless rotation can realize by normalizing a physical length and assume the time and z dependent phase factor to be $\exp[j2\pi v(t - \gamma z)]$, where v is the normalized frequency and γ is the normalized propagation constant. It will be negative for the backward propagation wave. The Faraday's law and Ampere's law can be written as below:

$$\nabla \times E = -j2\pi vH \tag{33}$$

$$\nabla \times H = j2\pi v\varepsilon_r E \tag{34}$$

The three dimensional field vectors E and H are scaled to the same magnitude in free space impedance. For magneto-optic effect, the general expression of relative permittivity tensor, ε_r is shown as follow:

$$\varepsilon_r = \begin{bmatrix} \varepsilon_{xx} & j\varepsilon_{xy} & j\varepsilon_{xz} \\ -j\varepsilon_{xy} & \varepsilon_{yy} & j\varepsilon_{yz} \\ -j\varepsilon_{xz} & -j\varepsilon_{yz} & \varepsilon_{zz} \end{bmatrix} \tag{35}$$

The first-order of magneto-optic effect denotes the coupled field components. The ε_{xy} is induced by a longitudinal magnetic induction (B_z) that gives an increment to the coupling between two transverse electric field components. The other two, ε_{xz} from the y-directed magnetization and ε_{yz} from x-directed produce an NRPS by coupling the longitudinal component (E_z) with one transcendental electric field component E_x and E_y, respectively. Since the element ε_{yz} can be treated similar to ε_{xz}, it can assume that $\varepsilon_{xy} = 0$ and $\varepsilon_{yz} = 0$ and only to analyze the NRPS induced by the transverse magnetic (TM) mode. For such modes, the longitudinal magnetic field component is missing ($H_z = 0$) and there are only three non-trivial components H_y, E_x and E_z.

$$\partial_z E_x - \partial_x E_z = -j2\pi vH_y \tag{36}$$

$$\begin{pmatrix} -\partial_z H_y \\ \partial_x H_y \end{pmatrix} = j2\pi v \begin{pmatrix} \varepsilon_{xx} & j\varepsilon_{xz} \\ -j\varepsilon_{xz} & \varepsilon_{zz} \end{pmatrix} \begin{pmatrix} E_x \\ E_z \end{pmatrix} \tag{37}$$

The Eq. 37 can be inverted as

$$\begin{pmatrix} E_x \\ E_z \end{pmatrix} = \frac{1}{j2\pi v} \frac{1}{\varepsilon_{xx}\varepsilon_{zz} - \varepsilon_{xz}^2} \begin{pmatrix} \varepsilon_{xx} & -j\varepsilon_{xz} \\ j\varepsilon_{xz} & \varepsilon_{zz} \end{pmatrix} \begin{pmatrix} -\partial_z H_y \\ \partial_x H_y \end{pmatrix} \tag{38}$$

By replacing Eq. (38) into Eq. (36), the differential equation for H_y component can be demonstrated as follow:

$$\partial_x^2 H_y - (2\pi v)^2 \left[\frac{\varepsilon_{zz}}{\varepsilon_{xx}} \gamma^2 - \left(\varepsilon_{zz} - \frac{\varepsilon_{xz}^2}{\varepsilon_{xx}} \right) \right] H_y = 0 \tag{39}$$

The properties of H_y are conserved and NRPS exists except for a minor modification to the propagation constant. The NRPS must be attributed to the coupling of the two electric fields at the magneto-optic material interfaces. By defining $\varepsilon_e = \varepsilon_{zz} - \frac{\varepsilon_{xz}^2}{\varepsilon_{xx}}$ and recalling the momentum conservation, the normalized transverse wave vector κ is explained

$$\kappa = +\sqrt{\frac{\varepsilon_{zz}}{\varepsilon_{xx}} \gamma^2 - \varepsilon_e} \tag{40}$$

From Eq. 38, the solution of magnetic field H_y can be separated to a forward wave and backward wave and take the form of

$$H_y^{(n)} = \{A_n exp[-2\pi\kappa_n(x - x_n)] + B_n exp[2\pi\kappa_n(x - x_n)]\} e^{-i2\pi v\gamma z} \tag{41}$$

The positive sign in Eq. 40 assures that the A_n term is for the forward wave with phase retardation along x direction. Subsequently, by using $\partial_z = -j2\pi v\gamma$ and substituting Eq. 41 for Eq. 38, the field E_z can be written as

$$E_z = \frac{1}{j\varepsilon_e} \left(\frac{1}{2\pi v} \partial_x H_y - \gamma \frac{\varepsilon_{xz}}{\varepsilon_{xx}} H_y \right) \tag{42}$$

At the interface between any two layers, both tangential field components E_z and H_y must be continuous, so

$$f^{(n)}(d_n) = f^{(n+1)}(0) \tag{43}$$

where

$$f^{(n)}(x) = \begin{pmatrix} \frac{1}{1} & \frac{1}{1} \\ \frac{1}{\varepsilon_e\left(-\kappa - \frac{\varepsilon_{xz}\gamma}{\varepsilon_{xx}}\right)} & \frac{1}{\varepsilon_e\left(\kappa - \frac{\varepsilon_{xz}\gamma}{\varepsilon_{xx}}\right)} \end{pmatrix} \begin{pmatrix} Aexp(-2\pi v\kappa x) \\ Bexp(+2\pi v\kappa x) \end{pmatrix}_{(n)} \tag{44}$$

The label (n) should be added to all of the local variables on the right hand side except for γ. The origin of x is chosen as the left boundary of the n-th layer. From Eq. 43, it is able to extract the transfer matrix S_n of the n-th layer, which relates to the weighted indices A_n and B_n with A_{n+1} and B_{n+1} by

$$\begin{pmatrix} A^{(n+1)} \\ B^{(n+1)} \end{pmatrix} = S_n \begin{pmatrix} A^{(n)} \\ B^{(n)} \end{pmatrix} \tag{45}$$

By simple algebraic manipulation, the transfer matrix can be written as

$$S_n = \frac{1}{2} \begin{pmatrix} (1+a-b)\exp(-\phi_n) & (1-a-b)\exp(\phi_n) \\ (1-a+b)\exp(-\phi_n) & (1+a+b)\exp(\phi_n) \end{pmatrix} \tag{46}$$

where the transverse phase delay in the n-th layer, $\phi_n = 2\pi\nu\kappa_n d_n$. The full expression of a and b describes the jumping process from layer n to layer $n+1$, which can be written as

$$a_{n,n+1} = \frac{\varepsilon_e^{(n+1)}\kappa_n}{\varepsilon_e^{(n)}\kappa_{n+1}} \tag{47}$$

and
$$b_{n,n+1} = \left(\frac{\varepsilon_{xz}^{(n+1)}}{\varepsilon_{xx}^{(n+1)}} - \frac{\varepsilon_e^{(n+1)}}{\varepsilon_e^{(n)}} \frac{\varepsilon_{xz}^{(n)}}{\varepsilon_{xx}^{(n)}} \right) \frac{\gamma}{\kappa_{n+1}}, \tag{48}$$

respectively. If $b = 0$, the above equation returns to the case of non-magnetized medium. A nonzero b breaks the time-reversal symmetry and gives an increment to the NRPS. Let us assume $A_0 = 1$ to normalize all the weighted indices. The reflection coefficient (R) and transmission coefficient (T) can be obtained from the cascaded transfer matrix $S_T = S_N S_{N-1} \dots S_1$ by

$$\begin{pmatrix} A_N \\ 0 \end{pmatrix} = S_T \begin{pmatrix} 1 \\ B_0 \end{pmatrix}. \tag{49}$$

In the two-port network indicated by the above equation, the physical meaning of $B_0 = \frac{S_{T,21}}{S_{T,22}}$ is the reflection coefficient, whose poles correspond to the guided modes that exponentially decay away from the cladding boundaries. Hence, in essence, the calculation of NRPS involves solving the equation $S_{T,22} = 0$ and to obtain the two roots γ corresponding to backward and forward propagating waves. Subsequently, the NRPSs of unit length are obtained by the difference of normalized propagation constants $\Delta\gamma$ by $NRPS = 2\pi\nu\Delta\gamma$.

3.5 Nonreciprocal guided-radiation mode conversion

When a magnetic field is applied transversely to the direction of light propagation in an optical waveguide, a nonreciprocal phase shift occurs and can be used in an interferometric configuration to result in unidirectional propagation. By using the nonreciprocal phase shift the nonreciprocal guided

mode to radiation mode conversion has been demonstrated. [18] Figure 2.3 shows the relationship of propagation constant between TE and TM mode. TM modes traveling in the magneto-optic waveguide have distinct propagation constants for the forward- and the backward-travelling waves owing to the nonreciprocal phase shift. By adjustment of waveguide parameters, the following relationship is satisfied as $\beta_b^y < \beta_c^x < \beta_f^y$, where β_f^y and β_b^y denote the propagation constants of the forward- and the backward-traveling TM modes respectively, and β_c^x denotes the cut-off of transverse electric (TE) modes. Only the backward-traveling TM modes can couple to the TE radiation modes so that the device acts as the TM-mode optical isolator.

Figure 2.3 The relationship of propagation constant.

3.6 Fabrication processes

The magneto-optic waveguide can be fabricated by using several techniques. In this section, several techniques will be described, that is, surface activated bonding, photosensitive adhesive bonding, plasma-enhanced chemical vapor deposition, spin coating, electron beam lithography, ultraviolet lithography, and etching.

3.6.1   Surface activated bonding

The surface activated bonding (SAB) process is used to clean the material surface. This process removes adsorbed atoms and compound layers, typically oxides, which stabilize the surface [19]. Therefore, after the cleaning process, the surfaces become unstable "active" states. The SAB process has been developed for wafer bonding at low temperature. The advantage of SAB is to directly bond a different kinds of material at room temperature. It will create new field of different materials, like a solar battery and a surface acoustic wave (SAW) filter.

At first, ions or atoms are bombarded at room temperature in an ultra-high vacuum as shown in figure 2.4. This process will remove the oxide film and contaminants on the bonding surface by Ar ions or atoms bombardment, then create dangling bond on bonding interface for the connection of atoms. Atomic level

bonding among dangling bonds is carried out by having the bonding interface contacted with each other in an ultra-high vacuum. By this process, bonding of different materials at room temperature is achieved, such as chemical compound semiconductors and the similar one which is normally hard to bond.

Figure 2.4 Schematic process flow of surface activated bonding technique.

3.6.2   Photosensitive adhesive bonding

Adhesive wafer bonding [20–22] uses an intermediate layer for bonding two substrates. The advantages of this approach are low temperature processing (the maximum temperature lower than 400°C), surface planarization, and tolerance to particles contamination. Regardless of the polymer materials for wafer bonding process, there are two important categories based on their behavior during bonding: one is represented by materials which become viscous and flow during bonding process while the second category is formed by material which remains rigid after baking process and subsequently during bonding. The two different behaviors are very important for wafer bonding due to their major impact on process results. The critical parameter for wafer bonding process is film thickness and uniformity across wafer surface.

The adhesive bonding has a simple process property and the ability to form micro structure with high aspect ratio. The intermediate layer is applied by spin-on, spray-on, screen-printing, embossing, dispensing, or block printing on one or two substrate surfaces. The adhesive thickness and spinning speed curve have been studied to generate a repeatable process that yields reliable film thickness across a substrate, with known film thickness uniformity. The procedural steps of adhesive bonding are divided as shown in figure 2.5.

The cleaning and pre-treatment of substrate surfaces is the first step for bonding technique in which there are three requirements. First, the weak boundary layer of the given material must be removed or chemically modified to create a strong boundary layer. Second, the surface energy of the adhered should be higher than that of the adhesive for good wetting. Lastly, the surface profile can be improved to provide mechanical interlocking. These techniques are available to help produce a desirable surface for adhesive bonding. The second step is to connect the adhesive layer. The most adhesive materials are polymers. The polymers enable to connect with different materials at low temperature. After that, these structures will be contracting with the substrate and hardening the adhesive layer.

Figure 2.5 Schematic process flow of photosensitive adhesive wafer bonding technique.

3.6.3   Plasma-enhanced chemical vapor deposition

Plasma-enhanced chemical vapor deposition (PECVD) [23] is a chemical vapor deposition (CVD) technology that utilizes a plasma to provide some of the energy for the deposition reaction to take place. The plasma, which is used in the PECVD technique, allows the usage of a wide range of precursors [24]. Plasma is a partially or fully ionized gas and generally is a mixture of electrons, charged particles, and neutral atoms. Therefore, the plasma state has high energy. The energy that is available in a plasma discharge is used for various applications, one of these applications is the deposition of thin films and coatings.

Figure 2.6 shows the PECVD process. An external energy source is required for the ionization of atoms and molecules, a pressure reduction system, and finally, the existence of a reaction chamber. The plasma induces radical or plasma polymerization in the monomers. Neutral molecules will be ionized or excited when the electrons and ions in the plasma interact with them, so they will become chemically reactive. The monomers that are used in this procedure are mainly in the gas or liquid states, which can be evaporated. Meanwhile, utilization of solid monomers requires inclusion of sublimation apparatus by which the solid monomer can sublime for deposition and this capability allows the use a vast range of materials as monomers [25]. When a gaseous or liquid precursor with high vapor pressure is introduced into the PECVD reaction chamber, dissociation, and activation of the precursor occur and in the presence of the plasma, which allows the deposition to happen at much lower temperatures compared to CVD. When the plasma comes in contact with the surface of a polymer substrate, modification of the surface can occur in different ways (etching). After that, the plasma treatment leads to the removal of materials from the surface (deposition) where precursors in the plasma stream are deposited as a plasma polymerized thin layer on the surface (cross-linking and functionalization), which involves modifications of the plasma polymers on the surface [26]. The advantages of the PECVD are operating at low temperature, low chances of cracking deposited layer, good dielectric properties of deposited layer, good step coverage, and less temperature dependent. [27]

Figure 2.6 Schematic of plasma-enhanced chemical vapor deposition technique.

3.6.4   Spin coating

Spin coating is a common method for coating the substrate with photoresists. In this technique, the few volume of the resist are dropped on a substrate, while the substrate is rotating with speed. Due to the centrifugal force, the dispensed resist spreads into a uniform resist film of desired film thickness, excess resist is spin off the edge of the substrate. At the same time, a part of the solvent evaporates from the resist film, so that its thinning stopped on the one hand and on the other hand, the resist film becomes sufficiently stable to suppress its elapsing during the handling of the wafers after coating.

3.6.5 Electron beam lithography

Electron beam lithography (EBL) is a process that uses electron beam (EB). EBL is one of the key fabrication techniques that allow us to create patterns at the nanoscale. The EBL working principle is relatively simple and very similar to photolithography: A focused beam of electron is scanned across a substrate covered by an electron-sensitive material (resist) that changes its solubility properties according to the energy deposited by the electron beam. Areas exposed, or not exposed according to the tone of the resist, are removed by developing.

EBL consists of a chamber, an electron gun, and a column. Column and chamber are maintained in high vacuum by a suitable set of pumps. The column contains all the electron optical elements needed to create a beam of electrons, to accelerate it to the working voltage, to turn it on and off, to focus, and to deflect it as required by the pattern to be written. The samples are normally loaded via a load lock into the main chamber and are typically placed on an interferometric stage for accurate positioning of the working piece. Figure 2.7 shows the computing system, the pattern generator, the operator interface, and all the electronics needed to control and operate the machine with EBL system.

Figure 2.7 Schematic of electron beam lithography.

3.6.6 Ultraviolet lithography

Photoresist is an organic polymer which changes its chemical structure when exposed to ultraviolet light. It contains a light-sensitive substance whose properties allow image transfer onto a print circuit board. There are 2 types of photoresist that included positive photoresist and negative photoresist as shown in figure 2.8. For positive resists, the exposed regions become more soluble and are thus more easily removed in the development

process. The net result is that the patterns formed (also called images) in the positive resist are the same as those on the mask. For negative resist, the exposed regions become less soluble and the patterns formed in the negative resist are the reverse of the mask patterns.

Figure 2.8 Schematic of ultraviolet lithography.

3.6.7   Etching

Etching is the process of using strong acid into remove material on the surface to create a design the pattern. Different etching processes are selected depending on the particular material to be removed. Etching is divided into "wet etching" and "dry etching" when chemical reactions of chemicals, reaction gases, and ions are used. Wet etching is a purely chemical process that removes material from a wafer using liquid-phase etchants. Dry etching is one of the most widely used processes in semiconductor manufacturing since it is easier to control, is capable of defining feature in small size, and produces highly anisotropic etching. It may remove the materials by chemical reactions, by purely physical method, or the combination of both chemical reaction and physical bombardment.

Reactive ion etching (RIE) is a directional etching process utilizing ion bombardment to remove material. RIE uses both physical and chemical mechanisms in order to achieve high levels of resolution. Figure 2.9 shows the RIE process. The process uses a chemically reactive plasma in a vacuum chamber to aggressively etch in a vertical direction. Horizontal etching is purposefully minimized in order to leave clean, accurate corners. RIE systems are used to remove organic material and etch away treated surfaces. Controlling ion density, electron temperature, and the plasma potential are of the utmost importance for ensuring a uniform etch. The chamber is set to vacuum. The electrode holds the materials to be treated and is electrically isolated from the vacuum chamber. Air or gas enters the chamber through a control valve on the front and is quickly evacuated by the vacuum pump installed in the rear. The type of gas used varies depending on a number of factors. Carbon tetrafluoride (CF_4) and oxygen are commonly used for etching.

Figure 2.9 Schematic of reactive ion etching.

References

[1] I. Newton, 1672, "**A letter of Mr. Isaac Newton, Professor of the Mathmaticks in the University of Cambridge; containing his new theory about light and colors: sent by the author to the publisher from Cambridge, Febr. 6. 1671/72; in order to be communicated to the R. Society,**" Philosophical Transactions of the Royal Society, Vol. 6, No. 80, pp. 3075-3087.

[2] P. Fara, 2015, "**Newton shows the light: a commentary on Newton (1672) 'A letter … containing his new theory about light and colors …',**" Philosophical Transactions of the royal society, Vol. 373, Issue 2039.

[3] C. Huygens, Treatise on Light, translated by S. P. Thompson, University of Chicago Press., 2005 (1678).

[4] A. A. Michelson, and E. W. Morley, 1887, "**On the Relative Motion of the Earth and the Luminiferous Ether,**" American J. of Sci., Vol. 34, pp. 333-345.

[5] D. B. Hoover, B. Williams, C. Williams, and C. Mitchell, 2008, "**Magnetic susceptibility, a better approach to defining garnets,**" J. of Gemmology, Vol. 31, No. 3/4, pp. 91-103.

[6] D. V. Manson, and C. M. Stockton, 1984, "**Pyrope-spessartine garnets with unusual color behavior,**" Gems and Gemology, Vol. 20, No. 4, p. 200-7.

[7] C. M. Stockton, and D. V. Manson, 1985, "**A proposed new classification for gem-quality garnets,**" Gems and Gemology, Vol. 21, No. 4, p. 205-18.

[8] I. Adamo, A. Pavese, I. Diella, and D. Ajo, 2007, "**Gem-quality garnets: correlations between gemological properties, chemical composition and infrared spectroscopy,**" J. of Gemmology, Vol. 30, No. 5/6, p. 307-319.

[9] S. Geller, 1967, "**Crystal chemistry of the garnet,**" Zeitschrift fur Kristallographie, Vol. 125, No. 125, pp. 1-47.

[10] M. N. Akhtar, A. B. Sulong, M. A. Khan, M. Ahmad, Ghulam M., M. R. Raza, R. Raza, M. Saleem, and M. Kashif, 2016, "**Structural and magnetic properties of yttrium iron garnet (YIG) and yttrium aluminum iron garnet (YAIG) nanoferrites prepared by microemulsion method,**" J. of Magnetism and Magnetic Material, Vol. 401, pp. 425-431.

[11] M. Gomi, K. Satoh, and M. Abe, 1988, "**Giant Faradeay Rotation of Ce-Substituted YIG Films Epitaxially Grown by RF Sputtering,**" Jpn. J. Phys., Vol. 27, p. L1536.

[12] A. Tate, T. Uno, S. Mino, A. Shibukawa, and T. Shintaku, 1996, "**Crystallinity of Ce Substituted YIG Films Prepared by RF Sputtering,**" Jpn. J. Appl. Phys., Vol. 35, pp. 3419-3425.

[13] M. Faraday, 1846, "**I. Experimental researches in electricity. -Nineteenth series,**" Philos. Trans. Roy. Soc. London 1, Vol. 136, pp. 1-20.

[14] T. Haider, 2017, "**A review of magneto-optic effects and its application,**" Int. J. of Elecctromagnetics and Applications, Vol. 7, pp. 17-24.

[15] I. M. Savukov, S. K. Lee, and M. V. Romalis, 2006, "**Optical detection of liquid-state NMR,**" Nature 442, pp. 1021-1024.

[16] G. Mayer, and R. Gires, 1963, "**The effect of an intense light beam on the index of refraction of liquids,**" C.R. Acad. Sci. Vol. 258, p. 2039.

[17] H. Zhou, J. Chee, J. Song, and G. Lo, 2012, "**Analytical calculation of nonreciprocal phase shifts and comparison analysis of enhanced magneto-optical waveguides on SOI platform,**" Opt. Exp., Vol. 20, No. 8, pp. 8256-8269.

[18] J. R. Vacca, 2006, "**Optical networking best practices handbook,**" Wiley-Interscience 1st edition, p. 151.

[19] H. Takagi, Y. Kurashima, and T. Suga, 2016, "**(invite) Surface activated wafer bonding: principle and current status,**" ECS. Trans., Vol. 75, No. 9, pp. 3-8.

[20] E. Cakmak, V. Dragoi, E. Capsuto, C. M. Ewen, and E. Pabo, 2010, "**Adhesive wafer bonding with photosensitive polymers for MEMS fabrication,**" Microsyst. Technol., Vol. 16, pp. 799-808.

[21] M. Yao, D. Yu, N. Zhao, J. Fan, Z. Xiao, and H. Ma, 2017, "**Development of wafer level hybrid bonding process using photosensitive adhesive and Cu pillar bump,**" 2017 China Semiconductor Tech. Int. Conference, Shanghai, Chaina.

[22] A. Polykov, M. Bartek, and J. N. Burghartz, 2005, "**Area- selective adhesive bonding using photosensitive BCB for WL CSP applications,**" J. of Electronic Packaging ASME, Vol. 127, pp. 7-11.

[23] http://www.plasma-therm.com/pecvd.html

[24] K. D. Anderson, J. M. Slocik, M. E. McConney, J. O. Enlow, R. Jakubiak, T. J. Bunning, R. R. Naik, and V. V. Tsukruk, 2009, "**Facile plasma-enhanced deposition of ultrathin cross linked amino acid films for conformal biometallization,**" Small, Vol. 5, No. 6, pp. 741–749.

[25] M. C. Vasudev, H. Koerner, K. M. Singh, B. P. Partlow, D. L. Kaplan, E. Gazit, T. J. Bunning, and R. R. Naik, 2014, "**Vertically aligned peptide nanostructures using plasma-enhanced chemical vapor deposition,**" Biomacromolecules, Vol. 15, No. 2, pp. 533–540.

[26] Y. Hamedani, P. Macha, T. J. Bunning, R. R. Naik, and M. C. Vasudev, 2016, "**Plasma-enhanced chemical vapor deposition: where we are and the outlook for the future,**" IntechOpen, chapter 10

[27] https://www.ece.umd.edu/class/enee416.F2007/GroupActivities/Presentation5.pdf

CHAPTER 3 MAGNETO-OPTIC WAVEGUIDES FABRICATED BY BONDING TECHNIQUE

3.1 Introduction

In this chapter, the optical isolator with the Si guiding layer fabricated by bonding techniques is described. In the magneto-optic waveguide of the optical isolator, the Si guiding layer is connected with the magnetic garnet cladding layer by bonding techniques. As for the bonding technique, surface activated bonding and photosensitive adhesive bonding are employed. The rib waveguides with the Si guiding layer are investigated for the optical isolator employing the nonreciprocal guided-radiation mode conversion. Preliminary experiments of the bonding techniques are discussed.

3.2 Device structure

An optical isolator employing a nonreciprocal guided-radiation mode conversion has been investigated. This device consists of a straight rib-type magneto-optic waveguide with a Si guiding layer. A magneto-optic waveguide in the optical isolator has a magnetic garnet / Si / SiO$_2$ structure, as shown in figure 3.1. A Ce:YIG is used as a magnetic garnet cladding layer. Ce:YIG has a Faraday rotation coefficient θ_F of approximately –4,500 deg/cm at 1.55 μm. The refractive indices of Ce:YIG, Si, SiO$_2$ are 2.22, 3.50, and 1.44, respectively at 1.55 μm. Nonreciprocal phase shifts represent unequal phase shifts for the forward and backward propagating waves in the magneto-optic waveguide; therefore, both waves exhibit distinct propagation constants. The differential equation of TM modes obtained from Maxwell's equations includes a nonzero linear term in the propagation constant β, which indicates that there are nonreciprocal solutions.
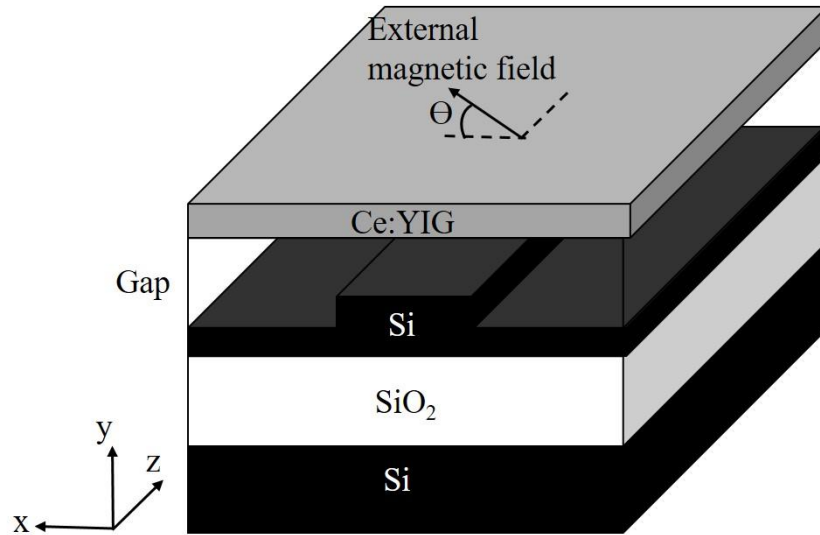
Figure 3.1 Optical isolator fabricated by bonding technique.

3.3 Isolator design

The magneto-optic waveguide with the Si guiding layer can be realized by bonding between Si and a magnetic garnet. The magneto-optic waveguides fabricated by surface activated bonding process and photosensitive adhesive bonding were compared. The optical isolator was designed at a wavelength of 1.55 μm. The relationship of waveguide parameters for isolator operation was clarified for the magneto-optic waveguide with various gaps between Si and the magnetic garnet.

3.3.1 Surface activated bonding

Figure 3.2 shows cross-section of the magneto-optic waveguide fabricated by surface activated bonding. Owing to the surface activated bonding, bonding between Si and Ce:YIG with no gaps can be expected.
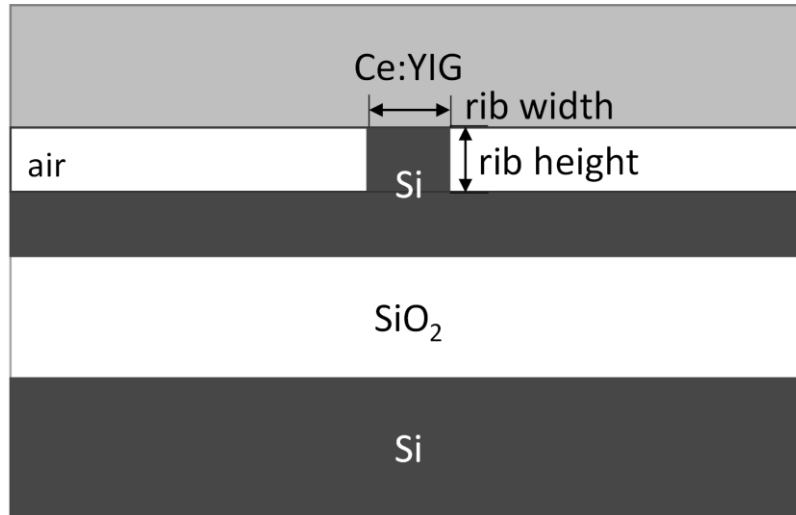
Figure 3.2 Cross-sectional structure of magneto-optic waveguide fabricated by surface activated bonding.

Figure 3.3 shows the calculated nonreciprocal phase shift as a function of thickness of the Si guiding layer. The magneto-optic waveguide has a structure of Ce:YIG/ gap (Air)/ Si/ SiO$_2$. When the gap between the magnetic cladding layer and Si is 0 nm, the magneto-optic waveguide exhibits the largest nonreciprocal phase shift. However, when the gap increases to 10 nm, 25 nm, and 50 nm, the Si guiding layer thickness for the largest nonreciprocal phase shift increases to 219 nm, 228 nm, and 238 nm, respectively. It is also seen from figure 3.3 that the amount of the nonreciprocal phase shift decreases as the gap increases. Similar to figure 3.3, figure 3.4 shows the relationship of waveguide geometric parameters, namely rib height and rib width at various gaps that satisfies propagation constant condition. Once the rib height is set, the range of the rib width for the isolator operation that satisfies follow propagation constant condition, is given. The filled and open circles represent the cases where β_f^y and β_c^x are equal and β_b^y and β_c^x are equal, respectively. The isolator operation is limited in the magneto-optic waveguide whose rib width ranges between filled and open circles. When the rib width is less than the filled circles, both the forward- and backward-traveling waves couple to the TE radiation modes. When the rib width is larger than the open circles, neither the forward- nor backward-traveling waves couple to the TE radiation modes. The impact of gap and rib dimensions on the waveguide tolerance is also demonstrated. For example, when the gap is 0 nm and the rib height is 79 nm, the rib width is ranged between 4.78 μm and 6.14 μm, that means there is a tolerance of 1.36 μm. When the gap is 10 nm and the rib height is 83 nm, the tolerance reduces to 0.4 μm.
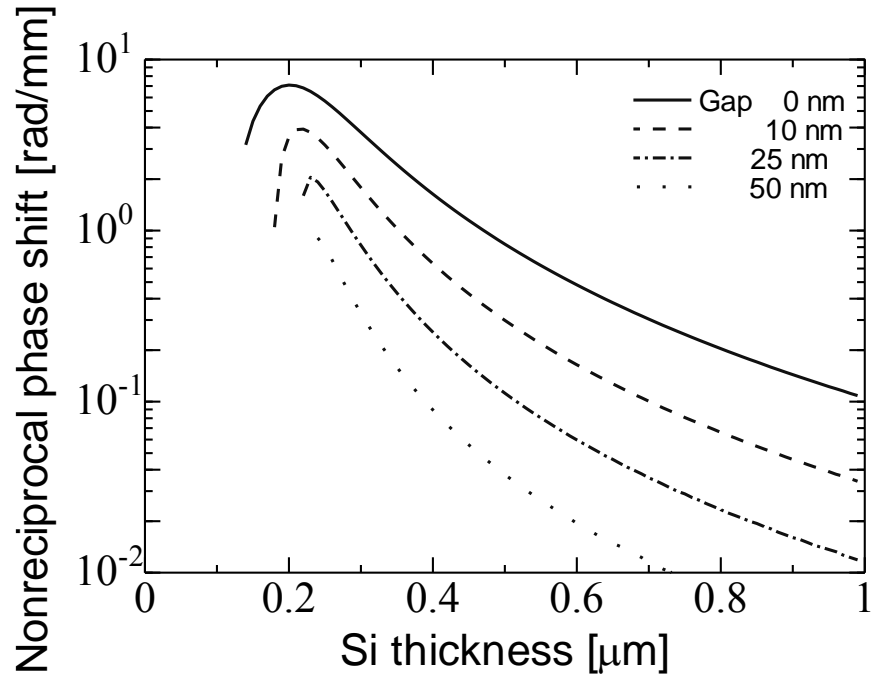
Figure 3.3 Calculated nonreciprocal phase shift depending on Si thickness when the waveguide is
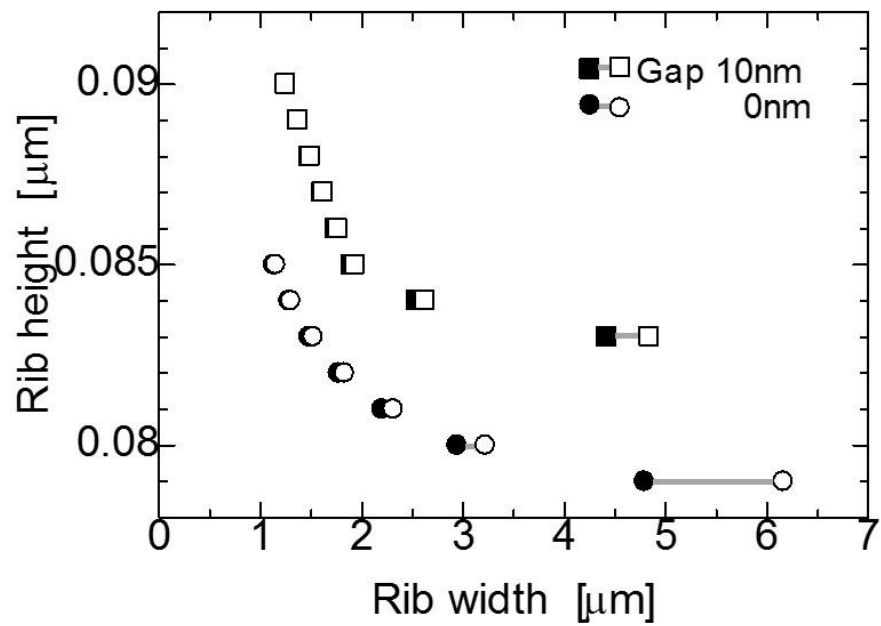
fabricated by surface activated bonding.

Figure 3.4 Relationship of waveguide parameters for isolator operation when the waveguide is fabricated by surface activated bonding.

3.3.2 Photosensitive adhesive bonding

Figure 3.5 shows cross-section of the magneto-optic waveguide fabricated by photosensitive adhesive bonding. The nonreciprocal phase shift in the magneto-optic waveguide is calculated at the wavelength of 1.55 µm.
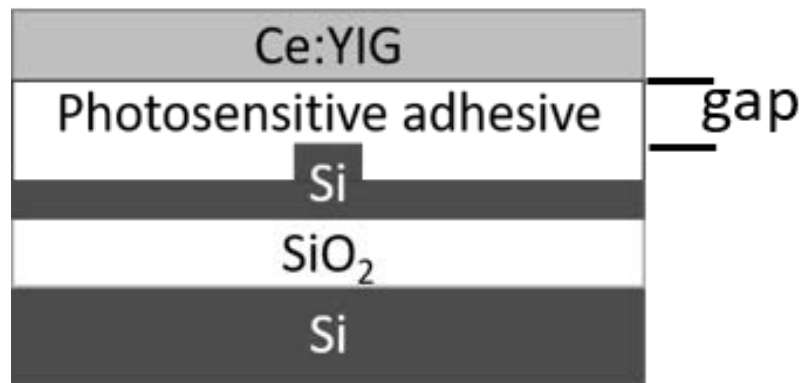

Figure 3.5 Cross-sectional structure of magneto-optic waveguides fabricated by photosensitive adhesive bonding.

Figure 3.6 shows the calculated nonreciprocal phase shift as a function of thickness of the Si guiding layer. When the gap between the magnetic cladding layer and Si is 0 nm, the thickness of the Si guiding layer for the maximum nonreciprocal phase shift is the same as that of the surface activated bonding. When the gap increases to 25 nm, 50 nm, and 100 nm, the Si guiding layer thickness for the largest nonreciprocal phase shift increases to 210 nm, 220 nm, and 230 nm, respectively. Figure 3.7 shows the relationship of the waveguide parameters that satisfies by propagation constant condition. When the gap is 0 nm and the rib height is 86 nm, the rib width is ranged between 2.26 µm and 2.38 µm, that means there is a tolerance of 120 nm. When the gap is 25 nm and the rib height is 99 nm, the tolerance reduces to 60 nm. Similar trends are confirmed for both magneto-optic waveguides.
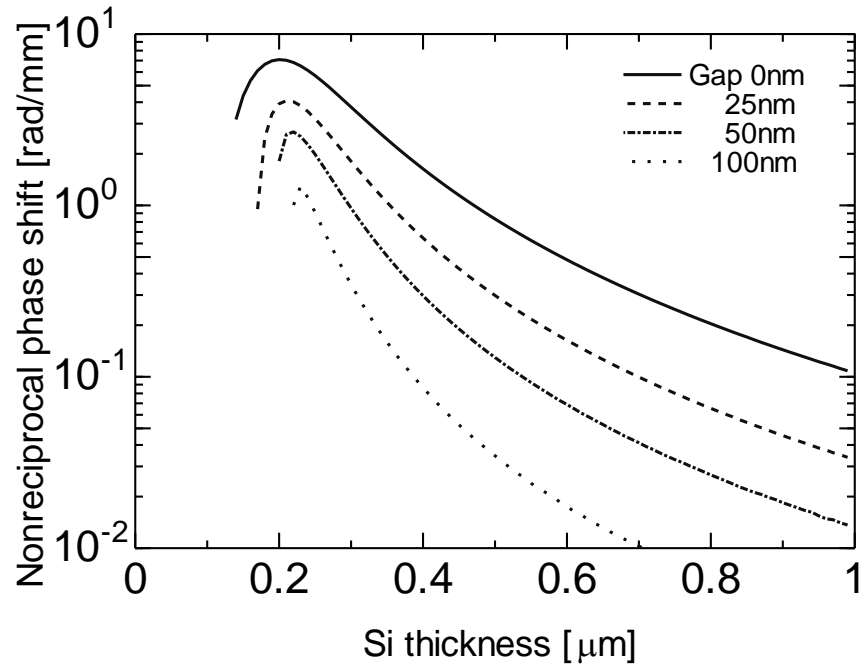
Figure 3.6 Calculated nonreciprocal phase shift depending on Si thickness when the waveguide is fabricated by photosensitive adhesive bonding.
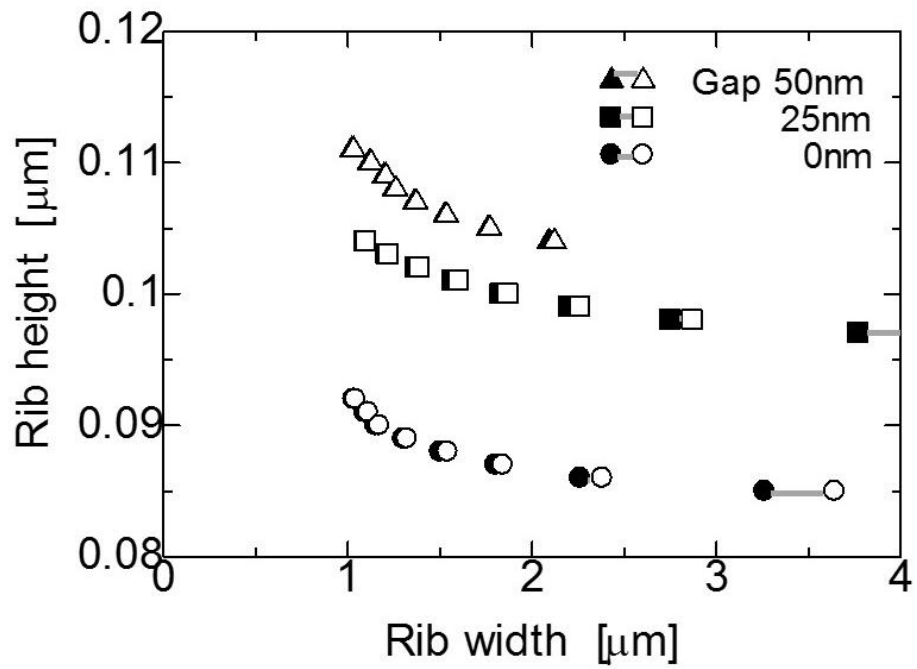
Figure 3.7 Relationship of waveguide parameters for isolator operation when the waveguide is fabricated by photosensitive adhesive bonding.

3.4 Calculation of isolation ratio

The isolation ratio of the optical isolator with Ce:YIG/ Si/ SiO$_2$/ Si structure is calculated. Figure 3.8 shows the cross-section of the magneto-optic waveguide with Si guiding layer. The isolation of the optical isolator employing the nonreciprocal guided-radiation mode conversion is calculated by simulating the electric field of TM guided mode and the electric field of TE radiation mode. The rib height and rib width are set equal to 0.097 μm and 6 μm, respectively for the isolator operation. For calculation, the boundary condition which defines the analysis region in the horizontal direction is located at (L) 5 μm. The equivalent refractive index (N_g) of this structure is 2.596431. The equivalent refractive index for TM mode in region 1 (n_{g1}) and 2 (n_{g2}) of this structure are 2.211418 and 2.585433, respectively. For TE mode, the equivalent refractive index in region 1 (n_{r1}) and 2 (n_{r2}) are 2.590765 and 2.965026 respectively.
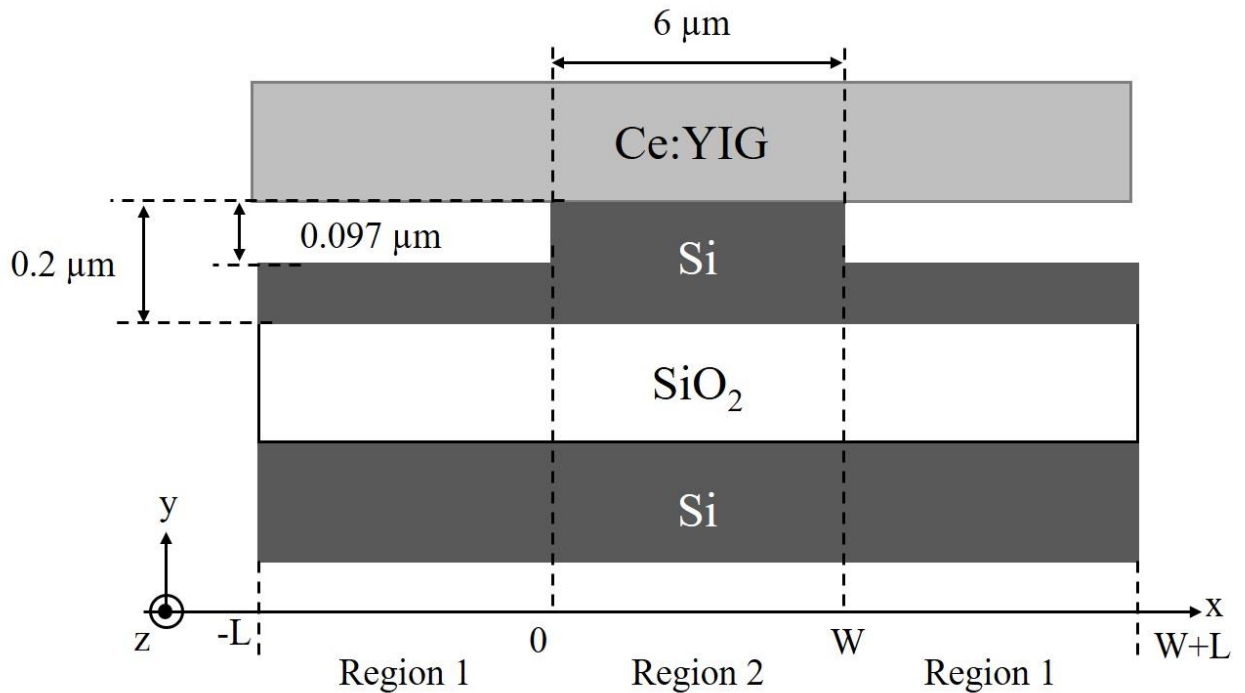

Figure 3.8 Cross-section of magneto-optic waveguide for calculating isolation ratio.

3.4.1 The electric field of TM guided mode

Following the structure, the electric field of TM guided mode (E_g) is simulated by COMSOL Multiphysics. The simulated electric field is shown in figure 3.9. The normalization equation of the electric field is explained as below:

$$E_{gy} = \begin{cases} (170.8256\ \exp(2.3r_1 x)) & ; x < 0 \\ (9.774\times 10^3\ \cos(0.535 j r_2 x + 1.55319)) & ; 0 < x < W \\ (170.8256\ \exp(-2.3r_1(x-W))) & ; W < x \end{cases} \quad (1)$$

Where E_{gy} is the electric field of the TM guided mode in y direction. $r_1 = k_0\sqrt{N_g^2 - n_{g1}^2}$, $r_2 = k_0\sqrt{n_{g2}^2 - N_g^2}$, and k_0 is the free space wave number given by $k_0 = \omega/c$.

The TM guided mode is normalized by this equation:

$$\tfrac{1}{4}\int (E_g^* \times H_g - H_g^* \times E_g).e_z dx = 1 \quad (2)$$

$$\int_{-\infty}^{\infty} (E_{gx}H_{gy} - E_{gy}H_{gx})dx = 2$$

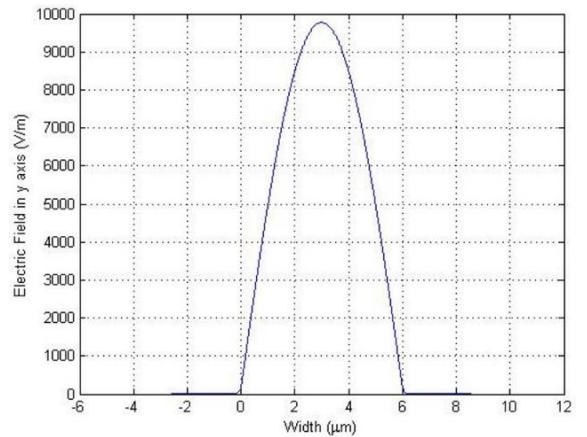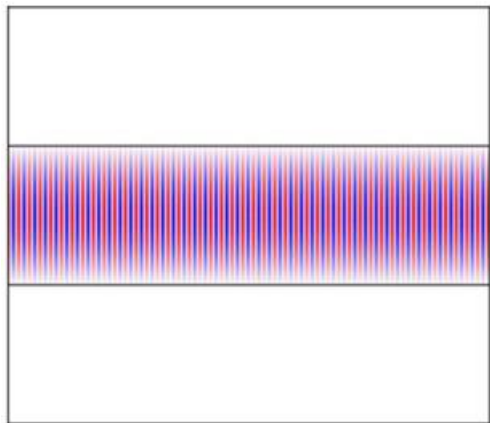$$\int_{-\infty}^{\infty} E_{gy}^2\, dx = \frac{2c\mu_0}{Ng}$$

Figure 3.9 The electric field of TM guided mode.

3.4.2 The electric field of TE radiation mode

Following this structure, the electric field of TE radiation mode (E_r) is simulated by COMSOL Multiphysics. The simulated electric field is shown in figure 3.10. The normalization equation of the electric field is explained as below:

$$E_{rx} = \begin{cases} 1.8623(|4.5k_1 x|\sin(3.9k_1 x) + 4) & ; x < 0 \\ 0.2673((1.2k_2(x-(\frac{W}{2}))) \sin(1.92k_2(x-(\frac{W}{2})))) & ; 0 < x < W \\ 1.8623((4.5k_1(x-W)) \sin(3.9k_1(x-W)) + 4) & ; W < x \end{cases} \quad (3)$$

Where E_{rx} is the electric field of the TE radiation mode in x direction. $k_1 = k_0\sqrt{n_{r1}^2 - N_r^2}$, $k_2 = k_0\sqrt{N_r^2 - n_{r2}^2}$, and $N_r = N_g$.

The TE radiation mode is normalized by this equation (width = 6.1 μm):

$$\frac{1}{4} \int (E_r^* \, x \, H_r - H_r^* \, x \, E_r). e_z dx = 1 \quad (4)$$

$$\int_{-\infty}^{\infty} (E_{rx}^* H_{ry}) dx = 2$$

$$\int_{-\infty}^{\infty} E_{rx}^* E_{rx} n(x)^2 \, dx = \frac{2c\varepsilon_0}{N_r}$$

Figure 3.10 The electric field of TE radiation mode.

3.4.3 The conversion of TM guided mode to TE radiation mode

The coupling coefficient of TM guided mode and TE radiation mode is given by

$$K(\beta) = \frac{1}{4}j\omega\varepsilon_0\frac{2N_g\theta_F}{k_0}\int_{-\infty}^{\infty}\left(-E_{gy}E_{rx}\sin\theta + E_{gy}E_{rz}\cos\theta\right)dx \tag{5}$$

Owing to the E_{rx} is larger than E_{rz}, the Faraday effect that depends on $\sin\theta$ rather than the nonreciprocal phase shift effect has a stronger influence on the coupling coefficient $K(\beta)$.

Therefore:

$$K(\beta) = \frac{1}{4}j\omega\varepsilon_0\frac{2N_g\theta_F}{k_0}\int_{-\infty}^{\infty}\left(-E_{gy}E_{rx}\sin\theta\right)dx \tag{6}$$

The radiation loss coefficient can be expressed by

$$2\alpha = 2\pi|K(\beta)|^2 \tag{7}$$

The power propagation in z direction is described as below

$$P(z) = P(0)\exp(-2\alpha z) \tag{8}$$

The power attenuation per unit can be calculated by

$$10\log_{10}\exp(-2\pi|K(\beta)|^2) \tag{9}$$

Figure 3.11 shows the calculation of the power attenuation as a function of an angle of the external magnetic field. The result shows that the power attenuation is increasing when θ increases. However, in order to generate the mode, the nonreciprocal phase shift is necessary to utilize the mode conversion. Since the nonreciprocal effect depends on θ, it must be as small as possible in order to obtain the largest nonreciprocal phase shift effect. From figure 3.11, the isolation ratio is approximately 15.6 dB/mm and 18.9 dB/mm at the angle of 40 $^{\circ}$ and 45 $^{\circ}$, respectively. When the angle is around 40-45 degrees, a very compact optical isolator can be realized.

Figure 3.11 The power attenuation of optical isolator depending on the angle of external magnetic field.

3.5 Fabrication processes

The fabrication process of the magneto-optic waveguide with Si guiding layer was demonstrated. The magnetic garnet and Si were connected with each other by bonding technique. The detail of the bonding techniques, that is surface activated bonding and photosensitive adhesive bonding, was explained.

3.5.1　Surface activated bonding

Preliminary experiment of surface activated bonding was conducted. Ar ion beam was irradiated over the surfaces of Si and Ce:YIG and then, the two wafers were bonded at room temperature. The atmosphere for bonding condition was 3×10^{-5} Pa in 3 minutes. Figure 3.12 shows a photograph of Si / Ce:YIG realized by surface activated bonding. Partial bonding between Si and Ce:YIG was confirmed, however, further experiment must be conducted for achieving intimate bonding.

Figure 3.12 Photograph of Si/ Ce:YIG fabricated by surface activated bonding.

3.5.2　Photosensitive adhesive bonding

The magneto-optic waveguide was fabricated by photosensitive adhesive bonding. The proposed optical isolator needs a layer of the adhesive material for bonding the magnetic garnet onto the Si guiding layer. TMMR N-A1000 by Tokyo Ohka Kogyo and a thinner are used as the photosensitive adhesive material and diluent, respectively. The temperature and pressure for bonding are approximately 160ºC and 600 g / cm^2, respectively. In the process, the adhesive can be diluted to reduce its thickness. The dilution consists of the thinner mixed with TMMR N-A1000. The dilution is dropped at a certain amount on the spinning SOI substrate that is placed in the chamber. Although it is difficult to adjust the thickness and uniformity of the adhesive owing to its viscosity, this type of adhesive ensures excellent chemical resistance to numerous acids, alkalines, and solvents. Pressure is applied to ensure intimate contact of the surfaces of the adhesive layer and the substrate. The dilution is then cured with ultraviolet (UV) light. A scanning electron microscope (SEM) is used to measure the adhesive layer thickness. Figure 3.13 shows the quadratic regression profile of adhesive layer thickness as a function of the percent dilution ratio. Note that at 2% dilution, that is, 1 part of the adhesive material: 49 parts of the diluents, the thickness of the adhesive layer is smallest at approximately 0.66 μm. If the adhesive material is diluted more than 49-fold, no bonding takes place. Therefore, by this technique, the adhesive layer thickness can be reduced to below 1 μm. Figure 3.14 shows the magneto-optic waveguide with a Ce:YIG/ TMMR N-A1000/ Si/ SiO$_2$ structure observed by using SEM.

Figure 3.13 Thickness of the adhesive layer as a function of dilution ratio.

Figure 3.14 Magneto-optic waveguide fabricated by photosensitive adhesive bonding.

3.6 Conclusion

The magneto-optic waveguide with a Si guiding layer fabricated by surface activated bonding and photosensitive adhesive bonding technique was investigated. For both waveguides, the nonreciprocal phase shift was calculated at a wavelength of 1.55 μm. The isolation ratio of the magneto-optic waveguide with Si guiding layer was simulated by the COMSOL Multiphysics program. By using the electric field of TM guided mode and that of TE radiation mode, the coupling coefficient of these modes were calculated. The isolation ratio depending on the angle of the external magnetic field was clarified. The waveguide parameters for isolator operation was considered for the magneto-optic waveguide with various gaps between Si and the magnetic garnet. Relationship of waveguide parameters were clarified for isolator operation.

References

[1]   H. Yokoi, T. Mizumoto, and Y. Shoji, 2003, "**Optical nonreciprocal devices with a Silicon guiding layer fabricated by wafer bonding**," Appl. Opt., Vol. 42, Issue 33, pp.6605-6612.

[2]   https://lemelson.mit.edu/resources/robert-hall

CHAPTER 4 MAGNETO-OPTIC WAVEGUIDES WITH a-Si:H GUIDING LAYER

4.1 Introduction

In this chapter, the optical isolator with the a-Si guiding layer is described. In the magneto-optic waveguide of the optical isolator, the a-Si guiding layer is deposited on the magnetic garnet cladding layer by PECVD. The rib waveguides with the Si guiding layer are investigated for the optical isolator employing the nonreciprocal guided-radiation mode conversion. The mathematical model of the electric field of TM guided mode and that of TE radiation mode are built in order to calculate the isolation ratio.

4.2 Device structure

Figure 4.1 shows an optical isolator with a-Si:H guiding layer deposited on a magnetic garnet cladding layer. Ce:YIG is used as a magnetic-garnet lower cladding layer. The refractive indices of Ce:YIG and a-Si:H are 2.22 and 3.48 respectively, at 1.55 μm. The optical isolator is comprised of a straight rib waveguide with the air/ a-Si:H/ Ce:YIG/ GCGMZG structure.
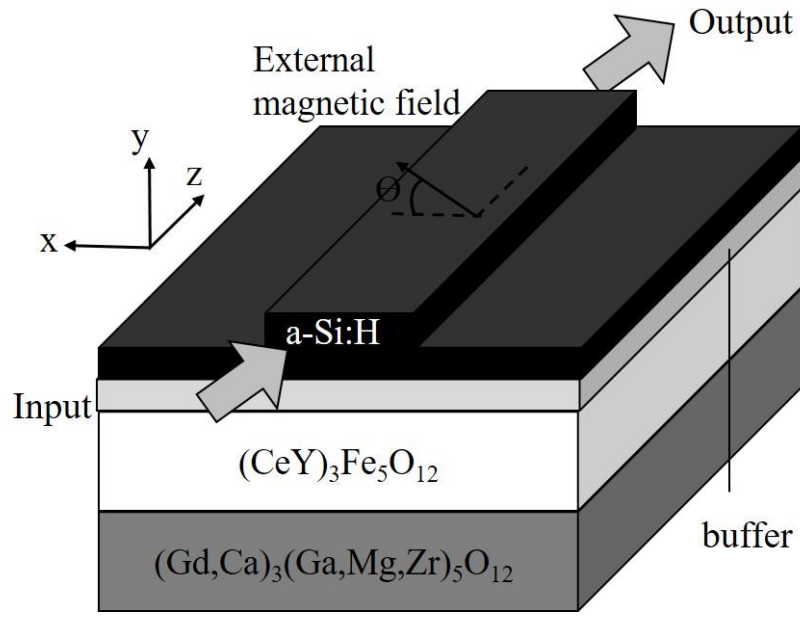
Figure 4.1 Optical isolator with a-Si:H guiding layer.

4.3 Isolator design

The optical isolator employing the nonreciprocal guided-radiation mode conversion is designed at the wavelength of 1.55 μm. Figure 4.2 shows the calculated nonreciprocal phase shift of the three-layer, air/ a-Si:H/ Ce:YIG, slab waveguide as a function of the a-Si:H thickness. It can be seen that at 0.22 μm a-Si:H thickness, the nonreciprocal phase shift obtains its maximum value. In this case, the thickness of the Ce:YIG cladding layer is assumed to be infinite in the air/ a-Si:H/ Ce:YIG waveguide. Figure 4.3 shows the calculated nonreciprocal phase shift of the four-layer, air/ a-Si:H/ Ce:YIG/ GCGMZG, slab waveguide as a function of the Ce:YIG thickness. The a-Si:H thickness of 0.22 μm obtained previously is selected. The calculation of the nonreciprocal phase shift indicates that the magnetic garnet of 0.5 μm thickness is sufficient to obtain the nonreciprocal phase shift equivalent to that of the infinitely thick magnetic garnet. Note that, if the optical isolator shown in figure 4.1 is taken to fabrication, the magnetic garnet cladding layer with a thickness greater than 0.5 μm will be required to achieve uniform nonreciprocal phase shift.
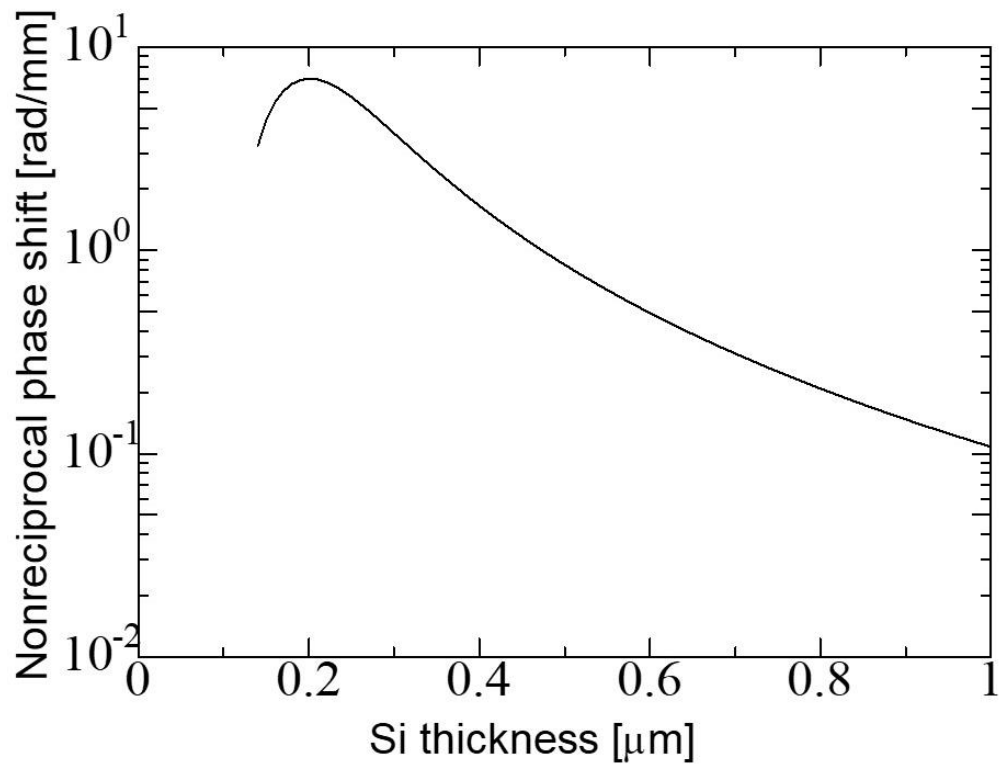
Figure 4.2 Calculated nonreciprocal phase shift for slab waveguide with air/ a-Si:H/ Ce:YIG structure depending on a-Si:H thickness.
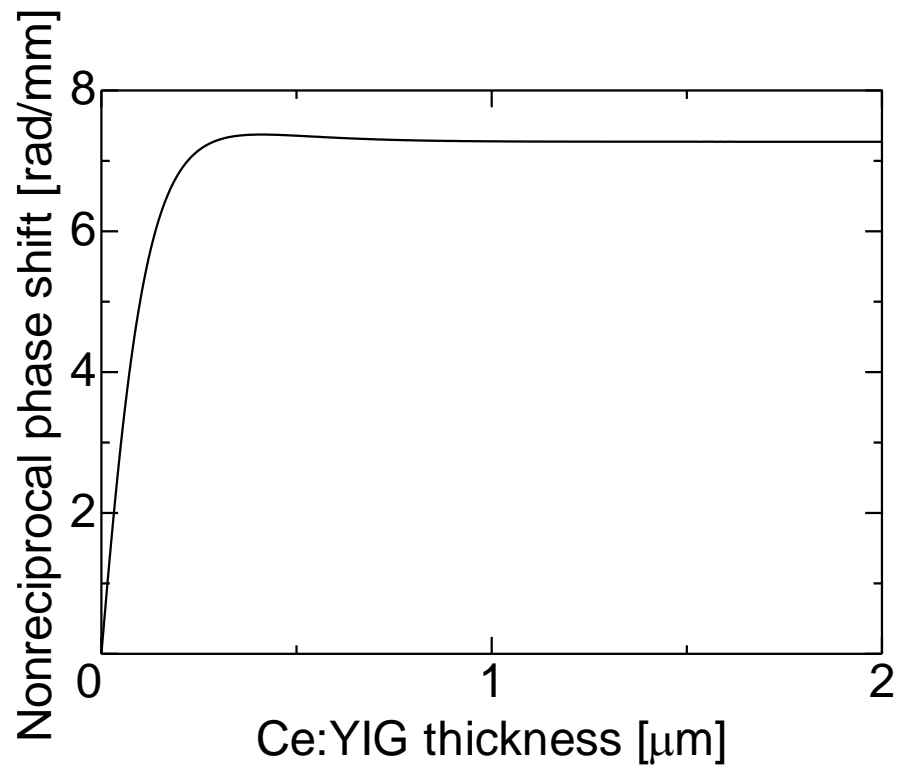
Figure 4.3 Calculated nonreciprocal phase shift for slab waveguide with air/ a-Si:H/ Ce:YIG/ GCGMZG structure depending on Ce:YIG thickness.

The optical isolator employing the nonreciprocal guided-radiation mode conversion is then designed at 1.55 μm. Figure 4.4 shows the cross-section of the magneto-optic waveguide in the optical isolator. The a-Si:H guiding layer thickness of 0.22 μm is selected in order to maximize the nonreciprocal phase shift. Figure 4.5 shows the relationship of the waveguide parameters that satisfies the condition of the propagation constants. Once the rib height is set, the range of the rib width for the isolator operation, which means that the propagation constants satisfy the relationship denoted by propagation constant condition, is given. The isolator operation is limited in the magneto-optic waveguide whose rib width ranges between filled marks and open marks.
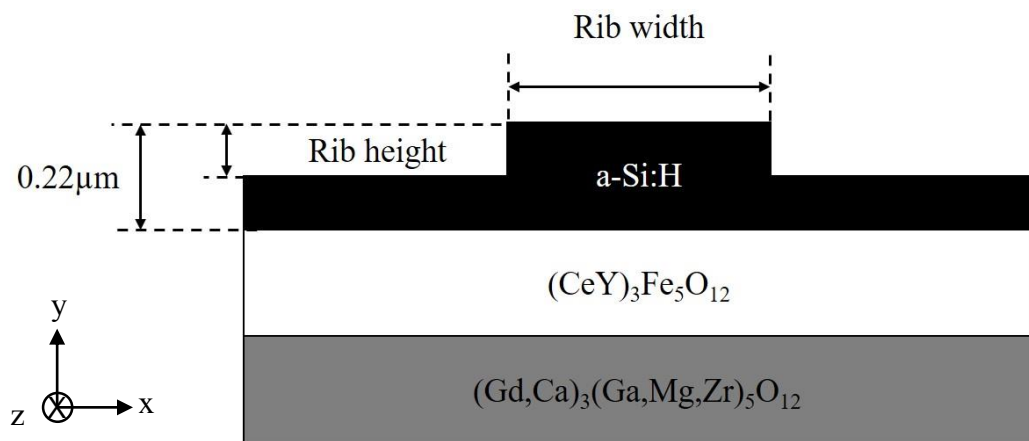
Figure 4.4 Cross-sectional structure of magneto-optic waveguide with a-Si:H guiding layer
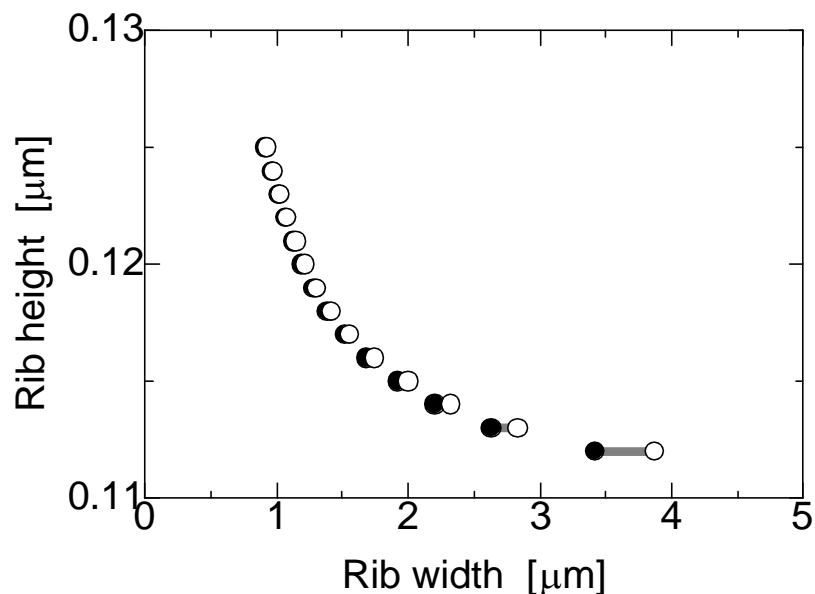
Figure 4.5 Relationship of waveguide parameters for isolator operation.

4.4 Calculation of isolation ratio

The isolation ratio of the optical isolator with air/ a-Si:H/ Ce:YIG structure is calculated. The cross-section of the magneto-optic waveguide is shown in figure 4.6. The isolation of the optical isolator employing the nonreciprocal guided-radiation mode conversion is calculated by simulating the electric field of TM guided mode and the electric field of TE radiation mode. The rib height and rib width are set equal to 0.11 μm and 2.1μm, respectively for the isolator operation. For calculation, the boundary condition which defines the analysis region in the horizontal direction is located at (L) 2μm. The equivalent refractive index (N_g) of this structure is 2.48431. The equivalent refractive index for TM mode in region 1 (n_{g1}) and 2 (n_{g2}) of this structure are 2.147758 and 2.481105, respectively. For TE mode, the equivalent refractive index in region 1 (n_{r1}) and 2 (n_{r2}) are 2.481165 and 2.484792, respectively.
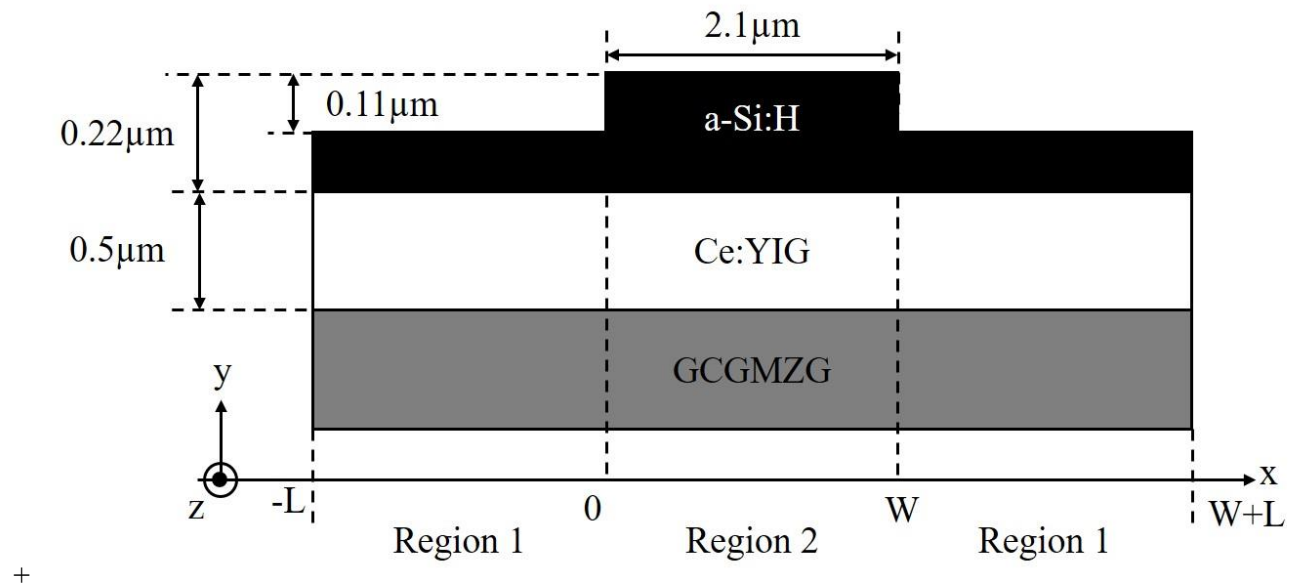

Figure 4.6 Cross-section of magneto-optic waveguide for calculating isolation ratio.

4.4.1 The electric field of TM guided mode

Following the structure, the electric field of TM guided mode (E_g) is simulated by COMSOL Multiphysics. The simulated electric field is shown in figure 4.7. The normalization equation of the electric field is explained as below:

$$E_{gy} = \begin{cases} (3.3205\times10^3 \exp(2.3r_1 x)) & ; x < 0 \\[2mm] (1.6249\times10^4 \cos(2.67jr_2(x-\frac{W}{2}))) & ; 0 < x < W \\[2mm] (3.3085e\times10^3 \exp(-2.3r_1(x-W))) & ; W < x \end{cases} \qquad (1)$$

Where E_{gy} is the electric field of the TM guided mode in y direction. $r_1 = k_0\sqrt{N_g^2 - n_{g1}^2}$, $r_2 = k_0\sqrt{n_{g2}^2 - N_g^2}$, and k_0 is the free space wave number given by $k_0 = \omega/c$.

The TM guided mode is normalized by this equation:

$$\frac{1}{4}\int (E_g^* \times H_g - H_g^* \times E_g).\, e_z dx = 1 \qquad (2)$$

$$\int_{-\infty}^{\infty} (E_{gx}H_{gy} - E_{gy}H_{gx})dx = 2$$

$$\int_{-\infty}^{\infty} E_{gy}^2\, dx = \frac{2c\mu_0}{Ng}$$
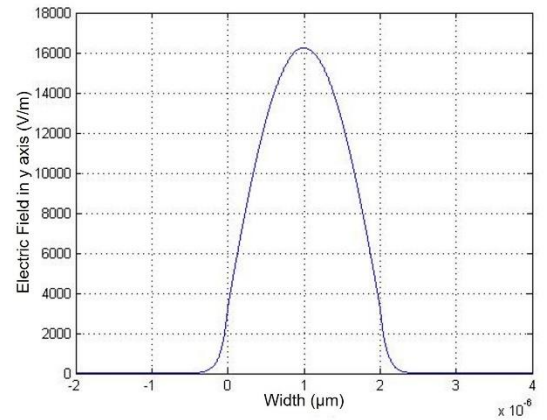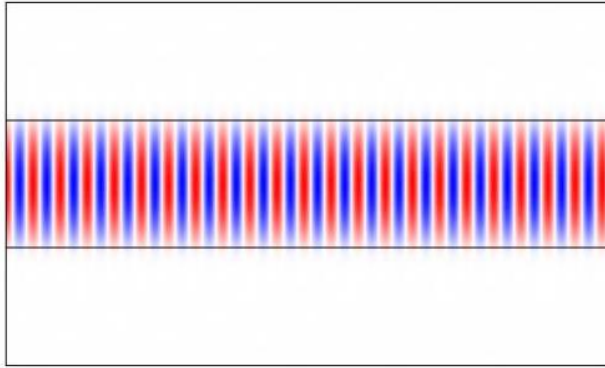

Figure 4.7 The electric field of TM guided mode.

4.4.2 The electric field of TE radiation mode

Following this structure, the electric field of TE radiation mode (E_r) is simulated by COMSOL Multiphysics. The simulated electric field is shown in figure 4.8. The normalization equation of the electric field is explained as below:

$$E_{rx} = \begin{cases} (3.604|2.59k_1 x\pi - 3| \sin(2.59k_1 x\pi - 3)) & ; x < 0 \\[2mm] (-3.4238((12\pi k_2(x-(\frac{W}{2}))) \sin(12\pi k_2(x-(\frac{W}{2}))))-8888) & ; 0 < x < W \quad (3) \\[2mm] (5.0456(2.59k_1\pi(x-W)) \sin(2.59k_1\pi(x-W))) & ; W < x \end{cases}$$

Where E_{rx} is the electric field of the TE radiation mode in x direction. $k_1 = k_0\sqrt{n_{r1}^2 - N_r^2}$, $k_2 = k_0\sqrt{N_r^2 - n_{r2}^2}$, and $N_r = N_g$.

The TE radiation mode is normalized by this equation (width = 6.1 µm):

$$\frac{1}{4}\int(E_r^* \times H_r - H_r^* \times E_r).e_z dx = 1 \qquad (4)$$

$$\int_{-\infty}^{\infty} \left(E_{rx}^* H_{ry}\right)dx = 2$$

$$\int_{-\infty}^{\infty} E_{rx}^* E_{rx} n(x)^2 \, dx = \frac{2c\varepsilon_0}{N_r}$$
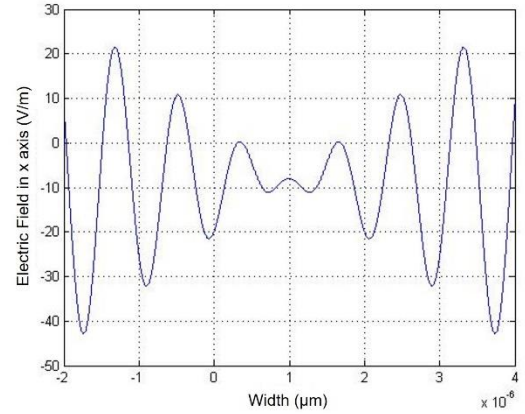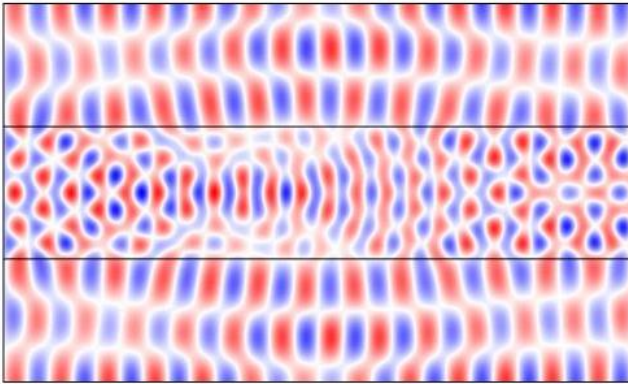

Figure 4.8 The electric field of TE radiation mode.

4.4.3 The conversion of TM guided mode to TE radiation mode

The coupling coefficient of TM guided mode and TE radiation mode is given by

$$K(\beta) = \frac{1}{4}j\omega\varepsilon_0 \frac{2N_g\theta_F}{k_0}\int_{-\infty}^{\infty}(-E_{gy}E_{rx}\sin\theta + E_{gy}E_{rz}\cos\theta)dx \qquad (5)$$

Owing to the E_{rx} is larger than E_{rz}, the Faraday effect that depends on $\sin \theta$ rather than the nonreciprocal phase shift effect has a stronger influence on the coupling coefficient $K(\beta)$.

Therefore:

$$K(\beta) = \frac{1}{4} j \omega \varepsilon_0 \frac{2 N_g \theta_F}{k_0} \int_{-\infty}^{\infty} (-E_{gy} E_{rx} \sin \theta) dx \qquad (6)$$

The radiation loss coefficient can be expressed by

$$2\alpha = 2\pi |K(\beta)|^2 \qquad (7)$$

The power propagation in z direction is described as below

$$P(z) = P(0) \exp(-2\alpha z) \qquad (8)$$

The power attenuation per unit can be calculated by

$$10 \log_{10} \exp(-2\pi |K(\beta)|^2) \qquad (9)$$

Figure 4.9 shows the calculation of the power attenuation as a function of an angle of the external magnetic field. The result shows that the power attenuation is increasing when θ increases. However, in order to generate the mode, the nonreciprocal phase shift is necessary to utilize the mode conversion. Since the nonreciprocal effect depends on θ, it must be as small as possible in order to obtain the largest nonreciprocal phase shift effect. From figure 4.9, the isolation ratio is approximately 0.90 dB/mm and 1.1 dB/mm at the angle of 40 ^{o} and 45 ^{o}, respectively. When the angle is around 40-45 degrees, a very compact optical isolator can be realized.
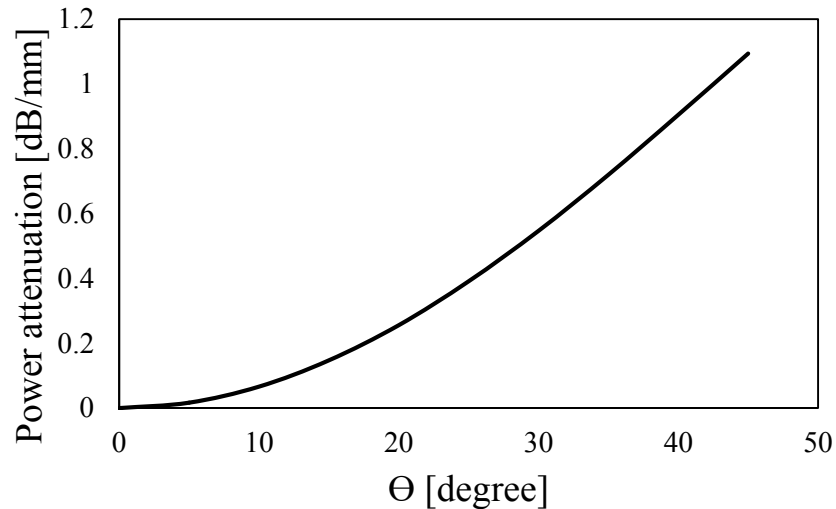

Figure 4.9 The power attenuation of optical isolator depending on the angle of external magnetic field.

4.5 Fabrication processes

The fabrication process of the nonreciprocal guided-radiation mode conversion with a-Si:H guiding layer is shown in the figure 4.10.
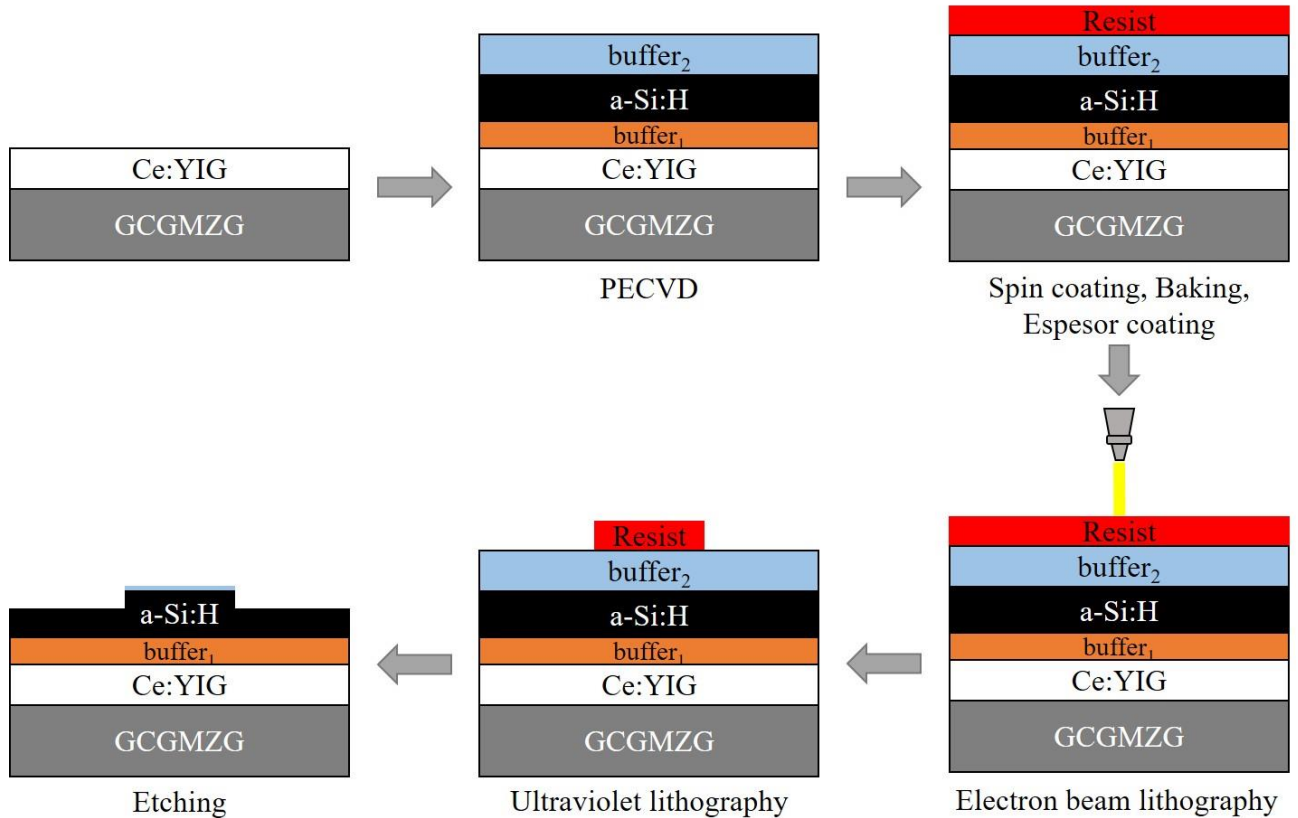
Figure 4.10 The fabrication process of the magneto-optic waveguide with a-Si:H guiding layer.

4.5.1 Plasma-enhanced chemical vapor deposition

The optical isolator with air/ a-Si:H/ Ce:YIG/ GCGMZG structure is fabricated by using the PECVD method to emit the a-Si:H guiding layer. The a-Si:H is incorporation of atomic hydrogen into the Si network. However, the material prepared in a way that contains a very high density of neutral threefold-coordinated Si dangling bonds, which prevent doping, carrier transport, and many other characteristics that are desirable for a useful optoelectronic device. The incorporation of hydrogen can decrease the Si dangling bonds. When the a-Si layer is deposited on the magnetic garnet, it is necessary to use the buffer layer. As for the buffer layer 1, Si nitride (SiN_x) is employed. Table 4.1 shows the conditions of PECVD process.

Table 4.1 PECVD's conditions

	Buffer 1	a-Si:H	Buffer 2
Thickness	50 nm	0.2 μm	50 nm
Gas flow	SiH$_4$S 5 sccm H$_2$ 8 sccm N$_2$ 500 sccm He 500 sccm	SiH$_4$ 100 sccm Ar 100 sccm	O$_2$ 300 sccm TEOS 2 sccm
Time	1 min 48 sec	11 min 3 sec	4 min
Power	50 W	100 W	120 W
Temperature	250 ºC	300 ºC	300 ºC

4.5.2 Spin coating, Baking, and Espesor

A spin coating is used for coated the resist layer. The coating film thickness control is determined by the viscosity of the resist, the acceleration of the disk, the rotation speed and time. In this study, ZEP 520A was used for resist. The spin's condition is shown in table 4.2.

Table 4.2 Spin coat's conditions

	Initial value	After accelerated
Speed	1000 rpm	6000 rpm
Time	3 sec	120 sec

Then, the substrate is heated in order to remove the solvent of the resist. Place the substrate on a hot plate and raise the temperature. The temperature is set to 180°C in 15 minutes. If the baking process is not performed, it will cause defects in the subsequent process.

A spin coater is used for applying the Espesor in the same manner as the resist coating. Spin coater initial conditions and after accelerated are shown in table 4.3.

Table 4.3 Espesor spin coat's conditions

	Initial value	After accelerated
Speed	300 rpm	1000 rpm
Time	3 sec	210 sec

4.5.3 Electron beam lithography

The resolution of the electron beam lithography technique is determined by the scattering of the electron beam. Since electrons are generally accelerated at high voltage, they are scattered by collisions with atoms constituting the resist. A part of the scattered electrons penetrates the resist layer and reaches the substrate. Electrons that have penetrated the resist layer and reached the substrate collide with atoms constituting the substrate. A part of the electrons scattered by the substrate bounces back to the resist layer and exposes the resist.

4.5.4 Ultraviolet lithography

The sensitivity of the resist depends on the type of solute and the temperature. The ZEP 520A is used as the solute in this research. It immerses the substrate in a solution to remove anything other than the necessary resist.

4.5.5 Etching

Reactive ion etching (RIE) is used in this research. Table 4.4 shows the RIE′s conditions. It uses a gas feed into a chamber in order to generating plasma (activation gas). Etching is performed by applying ions generated by separation of the gas to the wafer placed on the electrode.

Table 4.4 RIE′s conditions

Gas	CF_4	O_2	SF_6
Flow rate	20 sccm	20 sccm	3.5 sccm
Pressure	3.2 Torr	50 Torr	3 Torr

RF Power	10W	20 W	20 W
Time	24 min	2 min	2 min 4 sec

4.6 Evaluation of magneto-optic waveguide

The fabricated waveguide was observed by SEM. Figure 4.11 shows the cross-sectional SEM image of the magneto-optic waveguide with a-Si:H/ buffer/ Ce:YIG structure.
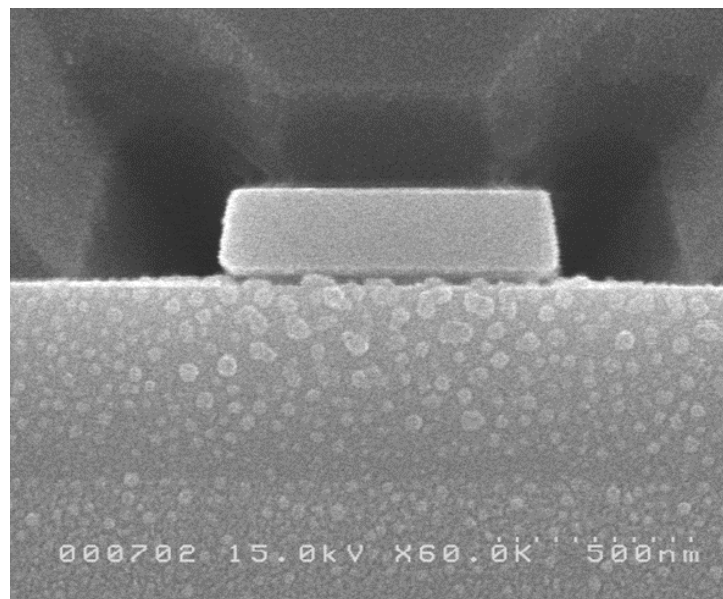

Figure 4.11 The magneto-optic waveguide with a-Si:H/ buffer/ Ce:YIG structure observed by SEM

Figure 4.12 shows the experimental setup for the optical waveguide. The lightwave from a tunable laser diode is launched into the fabricated waveguide via an optical fiber. The output from the waveguide is observed by a TV monitor through an infrared camera. The optical power is measured by an optical power meter. Figure 4.13 shows the near-field pattern observed at the output facet of the waveguide with a-Si:H guiding layer. It was confirmed that lightwave was well confined in the waveguide.
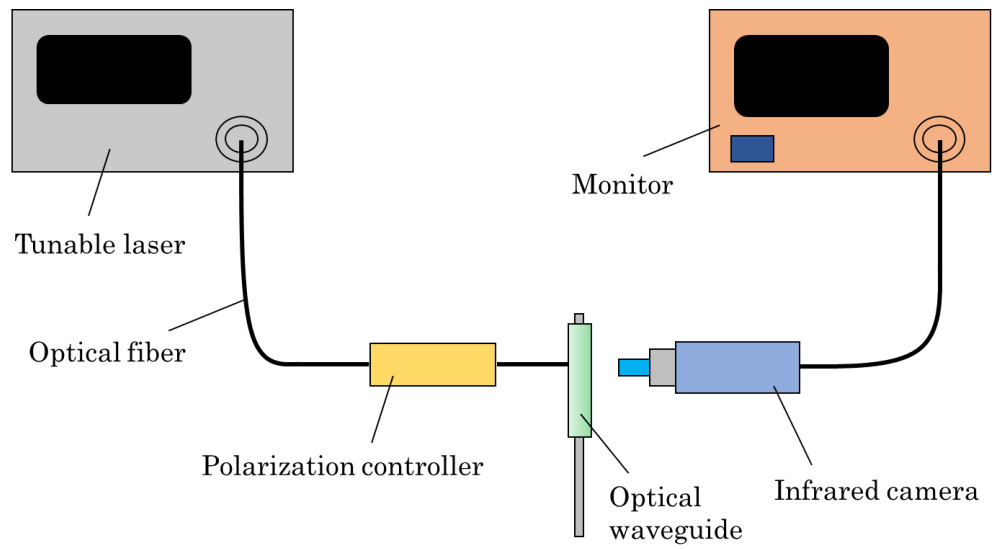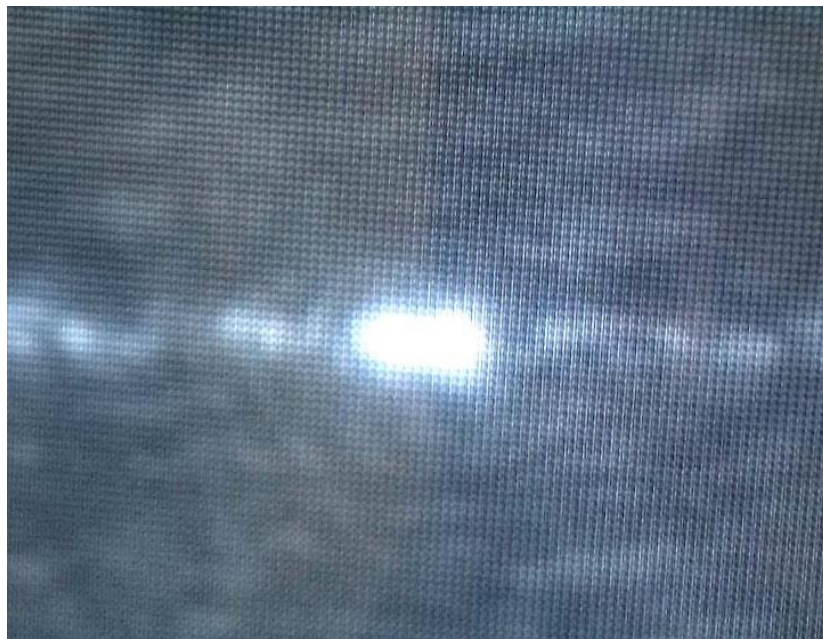
Figure 4.12 Experimental setup for optical waveguide.

Figure 4.13 Near-field pattern form the waveguide with a-Si:H guiding layer.

4.7 Conclusion

The magneto-optic waveguide with a-Si:H guiding layer was investigated. The nonreciprocal phase shift was calculated at a wavelength of 1.55 μm. The waveguide parameters for isolator operation was considered for the magneto-optic waveguide. Relationship of waveguide parameters were clarified for isolator operation. The isolation ratio of the magneto-optic waveguide with a-Si:H guiding layer was simulated by the COMSOL Multiphysics program. By using the electric field of TM guided mode and that of TE radiation mode, the coupling coefficient of these modes were calculated. The isolation ratio depending on the angle of the external magnetic field was clarified. The magnet-optic waveguide with a-Si:H/ buffer/ Ce:YIG/ GCGMZG structure was fabricated and evaluated.

CHAPTER 5 ATHERMAL OPERATION OF OPTICAL ISOLATOR

5.1 Introduction

There are no reports on the temperature dependence of the optical isolator employing the nonreciprocal guided-radiation mode conversion in rib type structure. The performance of the device may be deteriorated due to the temperature fluctuation because the effective refractive indices of the magneto-optic waveguides are dependent on the operating temperature. In this chapter, temperature dependence of the magneto-optic waveguide with the a-Si:H guiding layer is considered. Athermal condition of the magneto-optic waveguide with the a-Si:H guiding layer is proposed.

5.2 Temperature dependence of isolator design

The optical isolator with air/ a-Si:H/ Ce:YIG structure is designed at 1.55 µm at room temperature and temperature dependence of the optical isolator was investigated. Temperature dependences of the refractive indices are 1.86×10^{-4} |/K| and 2.5×10^{-4} |/K|, respectively, for a-Si:H and Ce:YIG. Temperature dependence of the magneto-optic coefficient $d\theta_F/dT$ is 13 deg/cm/K at room temperature [1]. Figure 5.1 shows relationship of waveguide parameters for isolator operation from 0ºC to 50ºC. It was found that the waveguide parameters were slightly shifted when the temperature was varied.
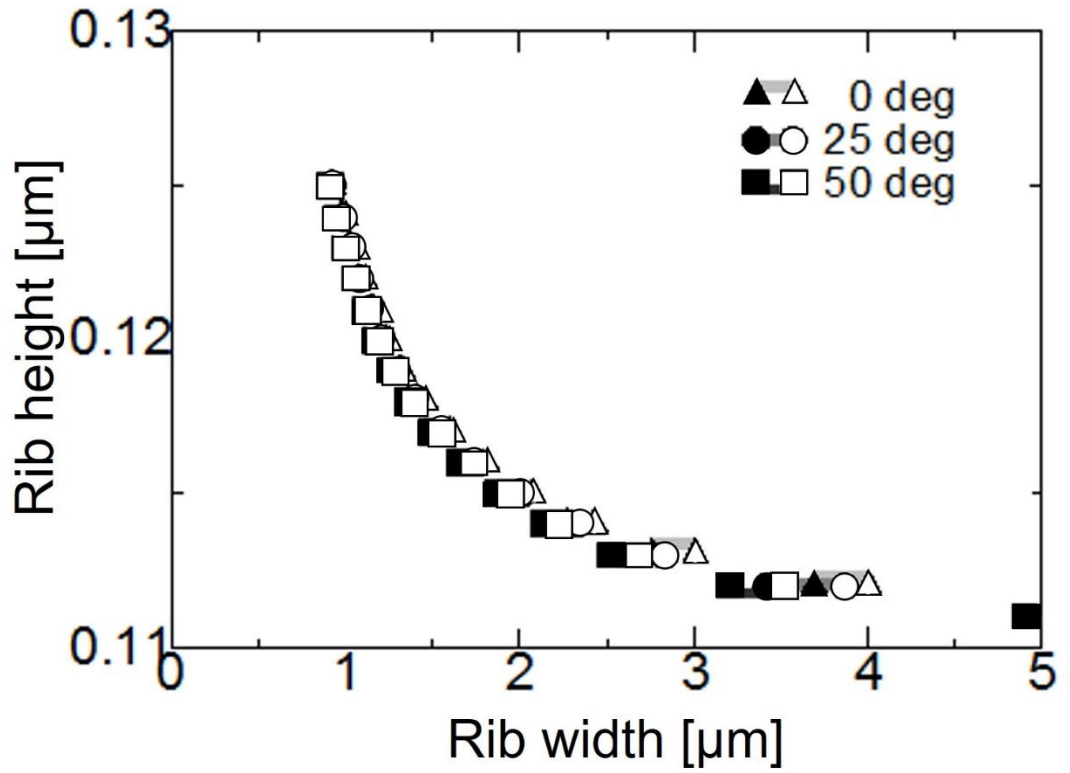
Figure 5.1 Relationship of waveguide parameters depending on operating temperature.

The athermal condition of the optical isolator employing the nonreciprocal guided-radiation mode conversion is next investigated. The magneto-optic waveguide structure comprising upper cladding/ a-Si:H/ Ce:YIG/ GCGMZG is considered. According to Yokoi and Sasaki [1], the refractive index of the upper cladding layer is varied usually between 1.0 and 3.0, and the large nonreciprocal phase shift is realized with the refractive index around 1.0 or 1.5. Therefore, in this paper, the refractive index of the upper cladding layer is assumed to be 1.5. At first, the temperature dependences of effective refractive indices are calculated. The temperature dependence of the refractive index of the upper cladding layer has a large impact on the shift of the relationship of waveguide parameters, which, in turn, affects the isolator operation. [2] The effective refractive index of the TM mode, n_{effTM}, is proportional to the TM mode propagation constant that is located between β_f^y and β_b^y. The effective refractive index of the TE cutoff mode, $n_{cutoffTE}$, is proportional to β_c^x. If n_{effTM} and $n_{cutoffTE}$ vary in a similar manner with the operating temperature, it is expected that the relationship expressed by propagation constant condition will be satisfied for a wide temperature range. Figure 5.2 shows n_{effTM} and $n_{cutoffTE}$ dependences on the operating temperature. The temperature dependence of the refractive index of the upper cladding layer

is assumed to be $\pm 5.0 \times 10^{-4}$ |/K| since the differences between n_{effTM} and $n_{cutoffTE}$ are small at these values. It is found that for the negative temperature dependence of the refractive index of the upper cladding layer, the difference in n_{effTM} and $n_{cutoffTE}$ is smaller than that for the positive temperature dependence of the refractive index of the upper cladding layer. The result suggests that the negative temperature dependence of the refractive index of the upper cladding layer is more effective for the athermal condition.
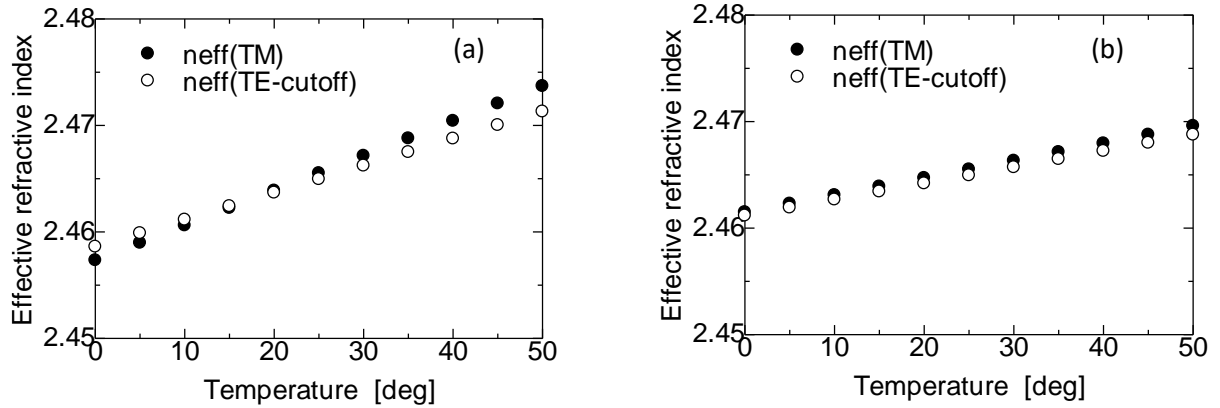

Figure 5.2 Effective refractive indices of TM mode and TE cutoff depending on the operating temperature. The temperature dependences of the refractive index of the upper cladding layer are assumed to be (a) $+5.0 \times 10^{-4}$ |/K| and (b) -5.0×10^{-4} |/K|.

Figure 5.3 shows n_{effTM} and $n_{cutoffTE}$ with the temperature dependences of the refractive index of -5.5×10^{-4}, -6.0×10^{-4}, -6.5×10^{-4}, and -7.0×10^{-4} |/K|. From the aforementioned refractive index temperature dependences, the average differences in effective refractive index are around 1.7×10^{-4}, 0.75×10^{-4}, 0.73×10^{-4}, and 0.77×10^{-4}, respectively. In these cases, it was found that the n_{effTM} and $n_{cutoffTE}$ with the refractive index temperature dependences of -6.0×10^{-4}, -6.5×10^{-4}, and -7.0×10^{-4} |/K| vary in a similar way. Figure 5.4 shows the relationship of waveguide parameters for magneto-optic waveguides with the upper cladding layer with the temperature dependences of the refractive index of $+6.0 \times 10^{-4}$, and -6.0×10^{-4} |/K|. For the latter case, the shift of the relationship of waveguide parameters for the isolator operation is negligible.
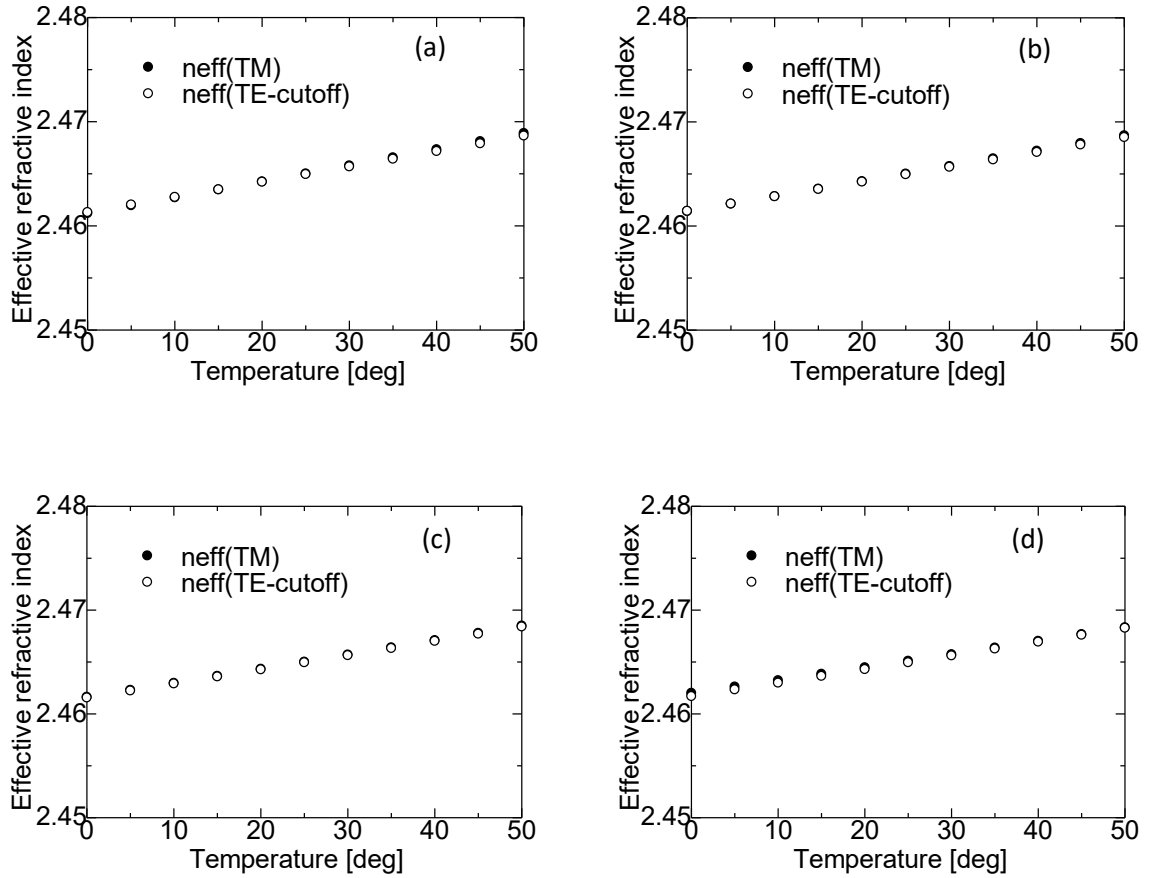
Figure 5.3 Effective refractive indices of TM mode and TE cutoff with the temperature dependences of the refractive index of (a) -5.5×10^{-4} |/K|, (b) -6.0×10^{-4} |/K|, (c) -6.5×10^{-4} |/K|, and (d) -7.0×10^{-4} |/K|.
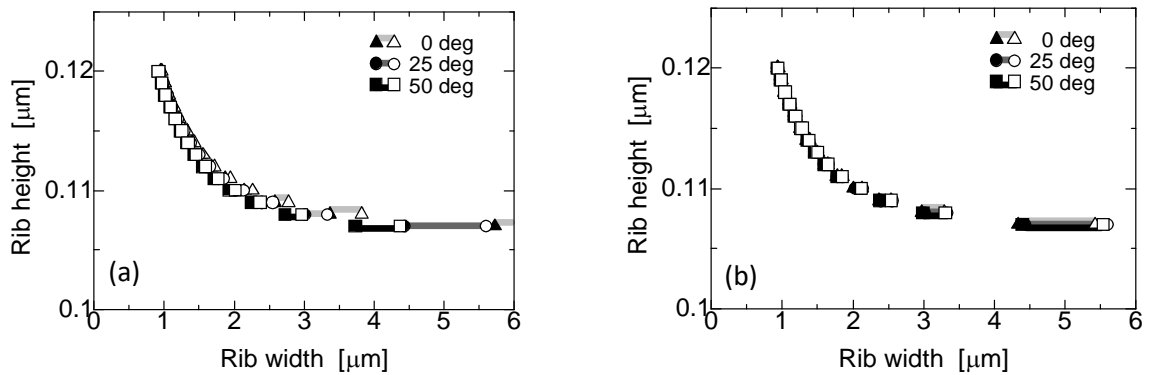

Figure 5.4 Relationship of waveguide parameters for magneto-optic waveguides with upper cladding layer when the temperature dependences of the refractive index are (a) $+6.0\times10^{-4}$ |/K|, and (b) -6.0×10^{-4} |/K|.

5.3 Material for upper cladding layer

The candidate material for the upper cladding layer is considered. From the above simulation, the results show that the investigated structure associated with the assumed refractive index of 1.5 for the upper cladding layer achieves the optimal temperature dependence of the refractive index of the upper cladding layer at -6.5×10^{-4} |/K|. It is found that there are 2 materials that possesses properties close to the simulated results. The first one is Titanium dioxide (TiO_2) [3] which has the refractive index of 2.13 and temperature dependence of the refractive index of -3×10^{-4} |/K|. Figure 5.5 shows the relationship of waveguide parameters for the magneto-optic waveguide with TiO_2. It is found that the TiO_2 can be used for the upper cladding layer for the athermal operation since the shifts of waveguide parameters are very small. The fabrication of the TiO_2/ a-Si:H/ Ce:YIG/ GCGMZG magneto-optic waveguide can be easily achieved by metal-organic chemical vapor deposition. [4]

The second one is methylcyclohexane ($C_6H_{11}CH_3$) compound [5], that has the refractive index of 1.4231 and temperature dependence of the refractive index of -5.018×10^{-4} |/K|. [6,7] Figure 5.6 shows the relationship of waveguide parameters for the magneto-optic waveguide with $C_6H_{11}CH_3$. The result shown in figure 5.6 indicates that the relationship of waveguide parameters for the isolator operation shifts only slightly. In order to achieve athermal operation of the optical isolator employing the nonreciprocal guided-radiation mode conversion, consideration of the effective refractive indices of the TM mode and TE cutoff is then significant. The fabrication of the $C_6H_{11}CH_3$/ a-Si:H/ Ce:YIG/ GCGMZG magneto-optic waveguide can be easily achieved by plasma-enhanced chemical vapor deposition method (PECVD). [7,8]
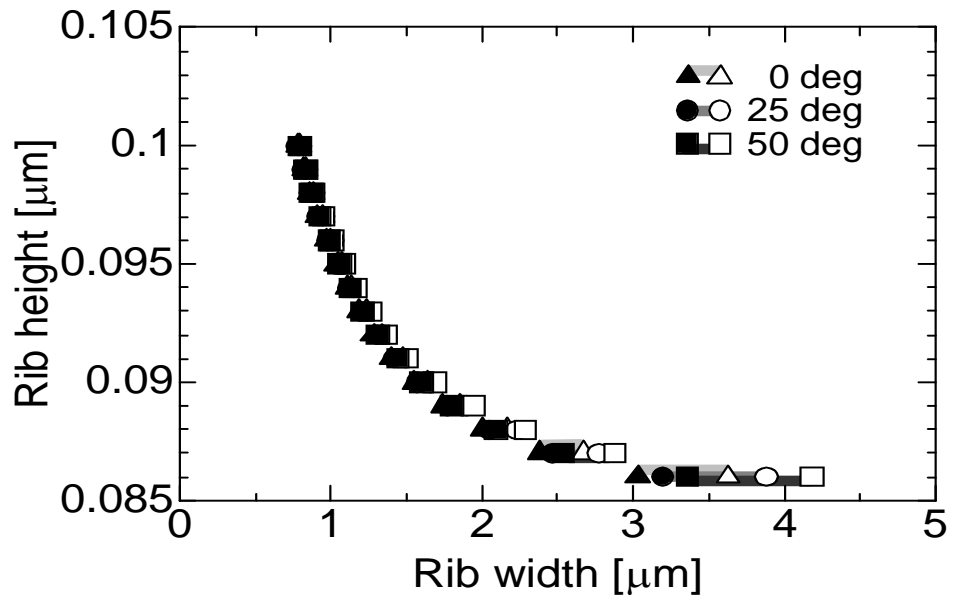
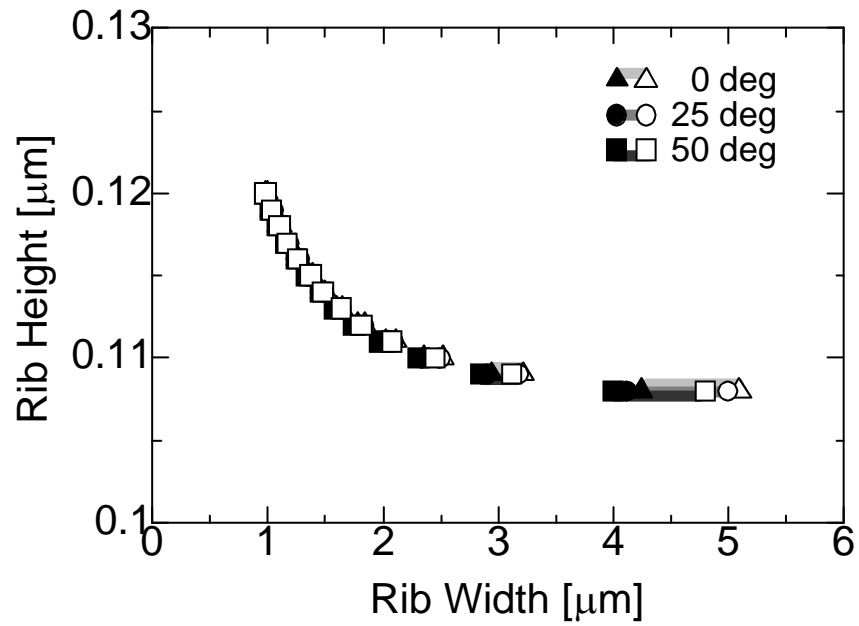Figure 5.5 Relationship of waveguide parameters for magneto-optic waveguides with TiO_2.

Figure 5.6 Relationship of waveguide parameters for magneto-optic waveguides with $C_6H_{11}CH_3$.

5.4 Conclusion

The temperature dependences of the optical isolator employing the nonreciprocal guided-radiation mode conversion was simulated by considering the effective refractive index of the TM mode and that of the TE cutoff mode. By selecting an appropriate material as an upper cladding layer, athermal condition of the magneto-optic waveguide can be achieved. The material for the upper cladding layer, that is close to the parameter of the simulated results, was proposed. The relationship of waveguide parameters for the magneto-optic waveguide with TiO_2 or $C_6H_{11}CH_3$ was clarified for their athermal operation. The TiO_2/ a-Si:H/ Ce:YIG/ GCGMZG magneto-optic waveguide can be fabricated by metal-organic chemical vapor deposition. Meanwhile, the $C_6H_{11}CH_3$/ a-Si:H/ Ce:YIG/ GCGMZG magneto-optic waveguide can be fabricated by PECVD method.

References

[1] H. Yokoi and K. Sasaki, 2008, "**Optical isolator with Si guiding layer fabricated by uv-activated bonding**," ECS Trans. 8 ed., Vol. 16., pp. 155-161.

[2] S. Choowitsakunlert, K. Kobayashi, K. Takagiwa, R. Silapunt, and H. Yokoi, 2016, "**Design of Optical Isolator Employing Nonreciprocal Radiation Mode Conversion for Athermal Operation**," presented at 21st Microoptics Conf., Berkeley, California, USA.

[3] J.-M. Lee, 2015, "**Athermal Silicon Photonics**," Silicon Photonics III: Systems and Application, (L. Pavesi and D. J. Lockwood), Chap. 3, pp. 83-97.

[4] M.-K. Lee, H.-C. Lee, C.-M. Hsu, 2006, "**High dielectric constant titanium oxide grown on amorphous silicon by metal-organic chemical vapour deposition**," Semiconductor Sci. and Tech., Vol. 21, Issue 5, pp. 604-607.

[5] Q. Wen, J. Shen, R. Gleleclak, K. H. Michaellan, J. H. Rohlling, N. G. C. Astrath, and M. L. Baesso, 2014, "**Temperature Coefficients of the Refractive Index for Complex Hydrocarbon Mixtures**," Int. J. Thermophys., Vol. **35**, Issue 5, pp. 930-941.

[6] https://pubchem.ncbi.nlm.nih.gov/compound/methylcyclohexane#section=Top

[7] K. Oda, K. Akamatsu, T. Sugawara, R. Kikuchi, A. Segawa, and S. Nakao, 2010, "**Dehydrogenation of Methylcyclohexane to Produce High-Purity Hydrogen using Membrane Reactors with Amorphous Silica Membrane**," Ind. Eng. Chem. Res. Vol. 49, pp. 11287-11293.

[8] M. Moreno, R. Ambrosio, Ar. Torres, Al. Torres, P. Rosales, A. Itzmoyotl, and M. Dominguez, , 2016, "**Amorphous, Polymorphous, and Microcrystalline Silicon Thin Films Deposited by Plasma at Low Temperature**," INTECH, Chap. 8, pp. 147-167.

CHAPTER 6 CONCLUSIONS

6.1 Conclusions

This research proposes an optical isolator employing the nonreciprocal guided-radiation mode conversion for Si photonics. The magneto-optic waveguide of the optical isolator has the Si guiding layer. Two types of the magneto-optic waveguide were investigated. One is the magneto-optic waveguide with the Si guiding layer by bonding technique. Surface activated bonding and photosensitive adhesive bonding were considered for bonding between Si and the magnetic garnet. The other is the magneto-optic waveguide with the a-Si:H guiding layer deposited on the magnetic garnet.

As for the magneto-optic waveguide fabricated by surface activated bonding, the nonreciprocal phase shift in the magneto-optic waveguide was calculated at the wavelength of 1.55 μm. Relationship of waveguide parameters for isolator operation was clarified. The simulation results show that the larger tolerance of the waveguide geometric parameters can be achieved at smaller gaps between Si and the magnetic garnet. As the preliminary experiment, surface activated bonding between Si and Ce:YIG was conducted. Successful bonding was achieved with the heat treatment at 25 °C. However, the surface activated bonding process is not reproducible at present.

As for the magneto-optic waveguide fabricated by photosensitive adhesive bonding, the nonreciprocal phase shift in the magneto-optic waveguide was calculated at the wavelength of 1.55 μm. Relationship of waveguide parameters for isolator operation was clarified. Similar tendency was confirmed for the magneto-optic waveguide fabricated by both bonding techniques. In order to obtain photosensitive adhesive bonding with smaller gap, dilution of the adhesive was studied. From the experimental results, at 2% dilution, that is, 1 part of the adhesive material and 49 parts of the diluents, the thickness of the adhesive layer is the smallest at approximately 0.66 μm. If the adhesive material is diluted more than 49-fold, no bonding takes place. Therefore, by this technique, the adhesive layer thickness can be reduced to below 1 μm. At this dilution, the photosensitive adhesive bonding is reproducible for the bonding between the magnetic garnet layer and guiding layer. However, this technique also has the drawback. It is difficult to predict the thickness of the adhesive layer during fabrication process.

The isolation ratio of the optical isolator with Ce:YIG/ Si/ SiO$_2$/ Si structure was calculated by simulating the electric field of TM guided mode and that of TE radiation mode. The COMSOL Multiphysics program was used in order to design mathematical model. It is confirmed that the power attenuation increases when the angle of the external magnetic field increases. When the angle of the magnetic field is 45 $^{\circ}$, 18.9 dB/mm isolation is obtained.

Moreover, the isolation ratio of the optical isolator with air/ a-Si:H/ Ce:YIG structure was calculated by simulating the electric field of TM guided mode and that of TE radiation mode. The COMSOL Multiphysics program was used in order to design mathematical model. It is confirmed that the power attenuation increases when the angle of the external magnetic field increases. When the angle of the magnetic field is 45 $^{\circ}$, 1.1 dB/mm isolation is obtained. The isolation ratio of both structures is different because of their equivalent refractive indices. The power attenuation of the optical isolator with a-Si:H guiding layer is lower than the power attenuation of the optical isolator with Si guiding layer. A waveguide isolator with high isolation ratio in a wider wavelength range is desired.

The magneto-optic waveguide with a-Si:H guiding layer was fabricated. The high quality a-Si:H layer was not deposited on the Ce:YIG directly. Therefore, Silicon Nitride (SiN$_x$), was used as a buffer layer between a-Si:H and Ce:YIG. The lightwave emitted from the laser diode was launched into the fabricated waveguide. The lightwave was well confined in the waveguide.

Temperature dependence of the optical isolator employing the nonreciprocal guided-radiation mode conversion was investigated. The optical isolator consists of the magneto-optic waveguide that has the air/ a-Si:H/ Ce:YIG/ GCGMZG structure. The refractive index of the upper cladding layer is assumed to be 1.5. The relationship of waveguide parameters for isolator operation was analyzed for various operating temperatures simulated by considering the effective refractive index of the TM mode (n_{effTM}) and that of the TE cutoff mode ($n_{cutoffTE}$). The temperature dependence of refractive index was considered in term of positive and negative value in order to study the relationship between n_{effTM} and $n_{cutoffTE}$. It was clarified that the athermal condition of the optical isolator employing the nonreciprocal guided-radiation mode conversion can be achieved when the upper cladding layer of the magneto-optic waveguide with the temperature dependence of the refractive index is equal to -6.5×10^{-4} |/K|.

For athermal operation, two candidates, TiO$_2$ and C$_6$H$_{11}$CH$_3$ compound were proposed for the upper cladding layer of the magneto-optic waveguide. For the magneto-optic waveguide with TiO$_2$ or C$_6$H$_{11}$CH$_3$ compound upper cladding layer, relationship of waveguide parameters for the isolator

operation was investigated. It was found that the shift for the isolator operation was very small for both magneto-optic waveguides. TiO_2 and $C_6H_{11}CH_3$ are promising candidates for the athermal operation of the optical isolator employing the nonreciprocal guided-radiation mode conversion.

6.2 Suggestions for the future work

The optical isolator employing nonreciprocal radiation mode conversion for silicon photonic has been studied for various applications that include the optical isolator with a Si guiding layer integrated with a garnet cladding on silicon-on-insulator (SOI) and the magneto-optic waveguides with a-Si:H guiding layer. There are several scopes to study about an optical isolator for Si photonics. In order to increase the efficiency of these structures, the research can be enhanced as follow:

The optical isolator with a magnetic garnet / Si / SiO_2 structure should be evaluated by the lightwave propagation in the waveguide. In addition, the optical isolator with an SOI substrate should be considered in term of the athermal operation. The temperature dependence of refractive indices should be considered to increase the performance of the device due to the temperature fluctuation. If this structure cannot operate in various temperature, this structure can be adjusted by changing the SiO_2 layer to another material.

The another structure is the magneto-optic waveguide with a-Si:H guiding layer employing the nonreciprocal phase shift. The upper cladding layer will embed on the optical isolator with a-Si:H/ Ce:YIG structure in order to achieve athermal operation. In addition, these structures will be evaluated by the lightwave propagation in the waveguide. The isolation ratio of the magneto-optic waveguide with a-Si:H guiding layer should be calculated by changing the upper cladding layer material. Moreover, the mathematical model should be developed or adapted to several kinds of material for the optical isolator employing the nonreciprocal guided-radiation mode conversion in rib type structure.